nature communications

Article

https://doi.org/10.1038/s41467-025-63659-w

AEBP1 drives fibroblast-mediated T cell dysfunction in tumors

Received: 22 August 2024

Accepted: 20 August 2025

Published online: 01 September 2025

Check for updates

Xiaoyu Wang[1,9], Jie Li[1,2,9], Daqiang Song[1,9], Yushen Wu[1,3,9], Jiazhou Liu[1,9], Ziying Yi[1], Jiazheng Sun[1], Jiefeng Huang[1,4], Linling Wu[1], Xiang Zhang[1], Jingyuan Wan[5], Li Zhang[6], Chong Li[7], Fan Li[1], Yuxian Wei[1], Yong Zhu[8], Huimin Du[3], Guosheng Ren[1] ✉ & Hongzhong Li[1] ✉

T cell dysfunction enables tumor immune evasion, understanding its mechanism is crucial for improving immunotherapy. Here we show, by RNA-sequencing analysis of human colon adenocarcinoma and triple-negative breast cancer tissues, that expression of Adipocyte Enhancer-Binding Protein 1 (AEBP1) positively correlates with T cell dysfunction and indicative of unfavorable patient outcomes. Subsequent single-cell RNA sequencing identifies cancer-associated fibroblasts (CAF) as the primary AEBP1 source. Fibroblast-specific AEBP1 deletion in mice enhances T cell cytotoxicity and suppresses tumor growth. Mechanistically, autocrine AEBP1 binds CKAP4 on CAFs, activating AKT/PD-L1 signaling to drive T cell dysfunction. By molecular-docking-based virtual screening we identify Chem-0199, a drug that disrupts the interaction between AEBP1 and CKAP4, thereby enhancing antitumor immunity. Both genetic and pharmacological AEBP1 inhibition synergize with immune checkpoint blockade in syngeneic models. Our study establishes AEBP1 as a key regulator of CAF-mediated T cell dysfunction and a therapeutic target.

T cell dysfunction in tumors is a complex process driven by various mechanisms operating within the tumor microenvironment (TME). One critical factor contributing to T cell dysfunction is the expression of immune checkpoint molecules on T cells, including programmed cell death protein 1 (PD-1) and cytotoxic T lymphocyte-associated protein 4 (CTLA-4)[1]. Interaction of these molecules with their ligands on tumor cells or other cells in the TME results in T cell exhaustion and decreased antitumor activity[2]. Moreover, cancer-associated fibroblasts (CAF) and other cells in the TME secrete immunosuppressive factors that further inhibit T cell function and hamper their ability to effectively target and eliminate tumor cells[3,4]. Additionally, the physical barriers created by CAFs and the extracellular matrix (ECM) in the TME also hinder T cell infiltration and migration towards the tumor site, exacerbating T cell dysfunction[5]. The interplay of these mechanisms creates a hostile TME, perpetuating tumor immune evasion and impeding the efficacy of immunotherapy interventions designed to boost T cell-mediated antitumor responses. Understanding and targeting these mechanisms are crucial for overcoming T cell dysfunction in the context of cancer.

[1]Department of Breast and Thyroid Surgery, Chongqing Key Laboratory of Molecular Oncology and Epigenetics, The First Affiliated Hospital of Chongqing Medical University, Chongqing, China. [2]Department of Dermatology, Shenzhen People's Hospital (The Second Clinical Medical College, Jinan University, The First Affiliated Hospital, Southern University of Science and Technology), Shenzhen, Guangdong, China. [3]Department of Oncology, The First Affiliated Hospital of Chongqing Medical University, Chongqing, China. [4]Department of Breast Surgery, Shenzhen People's Hospital (The Second Clinical Medical College, Jinan University, The First Affiliated Hospital, Southern University of Science and Technology), Shenzhen, Guangdong, China. [5]Department of Pharmacology, Chongqing Medical University, Chongqing, China. [6]Department of Pathophysiology, Chongqing Medical University, Chongqing, China. [7]Department of Oncology, The Affiliated Dazu's Hospital of Chongqing Medical University, Chongqing, China. [8]Research Institute of Life Sciences, Chongqing Medical University, Chongqing, China. [9]These authors contributed equally: Xiaoyu Wang, Jie Li, Daqiang Song, Yushen Wu, Jiazhou Liu.
✉e-mail: rengs726@126.com; lihongzhong@cqmu.edu.cn

Adipocyte enhancer-binding protein 1 (AEBP1), also known as aortic carboxypeptidase-like protein, is a secretory carboxypeptidase involved in various cellular processes, including adipogenesis, inflammation, and cancer progression[6,7]. In the context of tumors, AEBP1 functions as an oncogene, driving tumorigenesis and metastasis[8,9]. However, its impact on tumor immunity remains largely underexplored.

Our study reveals that AEBP1 is positively associated with T cell dysfunction and predominantly expressed in CAFs. By employing multiomics analyses and utilizing mice with fibroblast-specific gene ablation, we elucidates the pivotal role of AEBP1 in facilitating immune evasion mediated by CAFs. Inhibiting the AEBP1 pathway emerges as a promising approach to enhance the efficacy of immune checkpoint blockade therapy (ICT).

Results

Fibroblast-derived AEBP1 closely correlates with T cell dysfunction and poor patient survival

To investigate the mechanisms underlying T cell dysfunction, we conducted RNA-seq on 16 colon adenocarcinoma (COAD) and 14 triple-negative breast cancer (TNBC) samples (Fig. 1A). The Gene Set Variation Analysis (GSVA) scoring system was employed to assess the overall expression of genes related to T cell function within the transcriptome data. Based on the computed GSVA scores, the samples were stratified into two distinct categories: T cell activation and T cell dysfunction, reflecting the relative levels of T cell functional activity as inferred from the mRNA expression profiles (Supplementary Fig. 1A, B). By comparing the gene differences between the two categories, we identified 5 genes (*AEBP1, MMP2, MMP11, ISLR and SFRP4*) associated with T cell dysfunction. Then, we employed The Tumor Immune Dysfunction and Exclusion (TIDE) to further elucidate the association between these genes and T cell dysfunction. *AEBP1* exhibited the most robust association with T cell dysfunction in pan-cancer compared to other genes (Fig. 1B). Subsequent single-cell RNA sequencing (scRNA) analysis of COAD and TNBC samples based on Tumor Immune Single-cell Hub 2 (TISCH2) indicated the predominant expression of AEBP1 in human cancer-associated fibroblasts (hCAF) within the tumor microenvironment (TME) (Fig. 1C, D). Consistently, the dominant expression of AEBP1 in hCAFs was validated by double IF staining of AEBP1 and fibroblasts marker α-SMA in the tumor samples from two independent cohorts of cancer patients with COAD or TNBC (Fig. 1E, F). In both in-house cohorts, we observed a negative correlation between AEBP1 expression in hCAFs and the expression of Granzyme B (GZMB) in the TME, indicating a potential association between AEBP1 and T cell dysfunction (Fig. 1G, H). Finally, we performed survival analysis using the Kaplan-Meier Plotter to explore the correlation between AEBP1 expression and the clinical outcomes of cancer patients. Our findings revealed that individuals with lower *AEBP1* expression exhibited increased overall survival (OS) rates in cases of COAD or TNBC (Supplementary Fig. 1C, D). Consistent with this, our in-house COAD and TNBC cohort also demonstrated that patients with higher AEBP1 expression in tumors had shorter overall survival times (Fig. 1I, J). Together, our data showed that AEBP1 in hCAFs was positively associated with T cell dysfunction and closely related to poor prognosis of cancer patients.

Ablation of *Aebp1* in CAFs enhances T cell antitumor function

The clinical findings above suggested that AEBP1 in hCAFs may facilitate tumor progression by modulating T cell dysfunction. To elucidate this, we first investigated the direct impact of AEBP1 in CAFs on the proliferation and migration capacities of cancer cells. Co-culturing *AEBP1*-knockdown hCAFs, *Aebp1*-knockdown mouse CAFs (mCAF) or *Aebp1*$^{-/-}$ mCAFs with cancer cells, or treating cancer cells with recombinant mouse AEBP1 protein (rmAEBP1), did not exhibit more influence on growth and invasive potential of cancer cells in vitro, compared with matched controls (Supplementary Fig. 2A–F). Similarly, co-implantation of *Aebp1*-knockdown mCAFs with 4T1 mammary tumor cells in immunodeficient nude mice did not result in substantial changes in tumor growth and metastasis, compared to the counterpart group receiving control mCAFs and tumor cells (Supplementary Fig. 2G, H). In contrast, in immunocompetent mice, co-implantation of *Aebp1*-knockdown mCAFs with 4T1, CT26 colon tumor cells, or EMT6 mammary tumor cells led to slower tumor growth compared to control groups, suggesting *Aebp1* in mCAFs exerts pro-tumor activities by regulating T cell-based tumor immunity (Supplementary Fig. 2I–K).

To better clarify the relationship between CAF-derived AEBP1 and T cell function, we next crossed *Aebp1*$^{flox/flox}$ mice with the *S100a4*/fibroblast-specific protein 1 (*Fsp1*)^{Cre} strain to specifically deplete *Aebp1* on fibroblasts (hereafter *Aebp1*$^{flox/flox}$ denoted as wild type [WT] and *Aebp1*$^{flox/flox}$ *S100a4*^{Cre} as *Aebp1* cKO). The specific knockout of *Aebp1* in mCAFs was verified through genetic identification and western blot analysis (Supplementary Fig. 2L, M). The MC38 COAD cells, EO771 mammary tumor cells or B16-F10 melanoma cells were inoculated orthotopically into *Aebp1* cKO mice and WT mice. It was observed that all three types of tumors grew significantly slower in *Aebp1* cKO mice than in WT mice (Fig. 2A, B and Supplementary Fig. 2N). Subsequent flow cytometry analysis revealed an elevation in the levels of IFN-γ$^+$ and TNF-α$^+$ CD8$^+$ T cells in the tumors of *Aebp1* cKO mice as compared to WT mice (Fig. 2C, D and Supplementary Figs. 2O, 3A). Immunohistochemical (IHC) analysis of MC38 tumor-bearing mice demonstrated marked intensification of CD8a$^+$ and GZMB$^+$ signals in *Aebp1* cKO specimens relative to WT controls (Supplementary Fig. 3B), evidencing amplified cytotoxic lymphocyte (CTL) infiltration within TME. Furthermore, the TIDE database analysis revealed a critical dichotomy: while elevated CTL infiltration strongly correlated with improved OS in *AEBP1*-low COAD and TNBC, this survival advantage was completely abrogated in *AEBP1*-high cases (Supplementary Fig. 3C, D). This suggested that AEBP1 functionally compromise the prognostic benefit of tumor-infiltrating lymphocytes, consistent with our proposed mechanism of AEBP1-driven T cell dysfunction.

Moreover, enhanced infiltration of CD8$^+$ T cells was showed in tumors from *Aebp1* cKO mice compared to those from WT mice (Fig. 2E, F and Supplementary Fig. 3A). Similar results were also observed in 4T1, EMT6 or CT26 tumors co-implanted with *Aebp1*-knockdown mCAFs compared to those co-implanted with control mCAFs (Supplementary Fig. 3E, F). Furthermore, in our in-house TNBC cohort, an inverse correlation was identified between AEBP1 expression levels in hCAFs and the expression of CD8a in the TME (Supplementary Fig. 3G). Using a TNBC tissue microarray (n = 70), our multiplex immunofluorescence analysis revealed close spatial proximity between CD8$^+$ T cells and AEBP1-expressing CAFs within the TME (Fig. 2G). This spatial interaction was further contextualized by our quantitative findings showing a moderate inverse correlation between high AEBP1 expression and total CD8$^+$ T cell infiltration levels and cytotoxic GZMB$^+$ CD8$^+$ T cell subpopulations compared to low AEBP1-expressing samples (Fig. 2H). These observations supported the hypothesis that CAF-derived AEBP1 fosters T cell dysfunction through localized immunosuppression. Notably, the inhibition of tumor growth in *Aebp1* cKO mice was reversed by depleting CD8$^+$ T cells with anti-CD8 antibodies (Fig. 2I), indicating that the enhanced antitumor activity by *Aebp1* blockade is dependent on CD8$^+$ T cells.

To evaluate the overall influence of *Aebp1* blockade on the tumor immune landscape, we characterized CD45$^+$ immune cells isolated from MC38 tumor tissues in both WT and *Aebp1* cKO mice through mass cytometry (CyTOF). We identified a total of 10 distinct cell clusters (Supplementary Fig. 3H, I). MC38 tumors from *Aebp1* cKO mice had significantly increased CD8$^+$ T cells (cluster 1), whereas immunosuppressive immune cells like M2 macrophages (cluster 6) was decreased in tumors from *Aebp1* cKO mice (Fig. 2J, K), suggesting enhanced antitumor immunity.

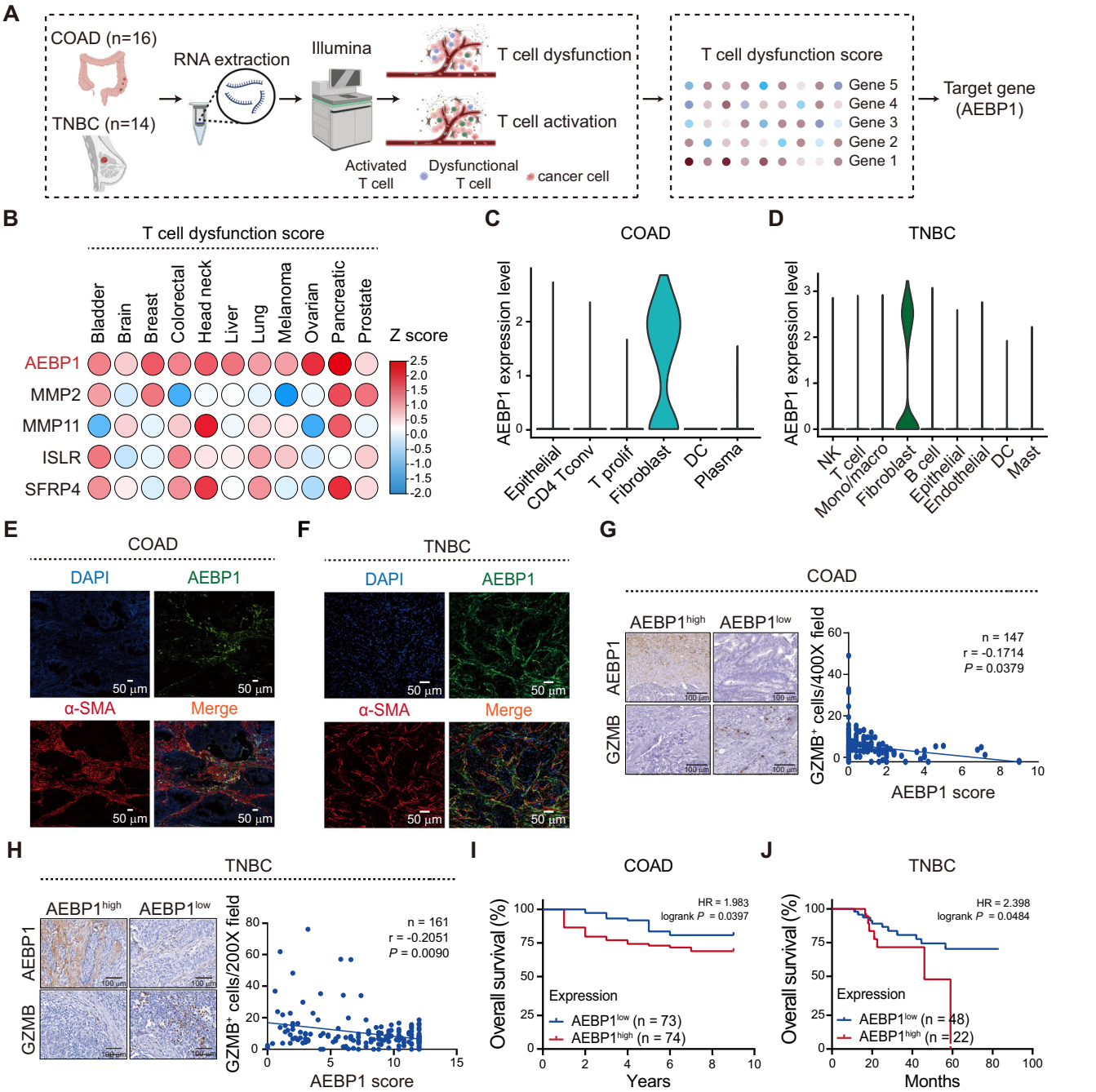

Fig. 1 | CAF-derived AEBP1 is associated with T cell dysfunction and closely related to poor survival. A Illustration of the workflow, including the cohorts of tumor samples and an overview of analytical approaches used. Created in BioRender. Xiaoyu, W. (2025) https://BioRender.com/5uvgprp. **B** T cell dysfunction scores of indicated genes in pan-cancer based on TIDE system. **C** Expression levels of *AEBP1* in the cell clusters in TME based on scRNA-seq data from COAD (CRC_GSE146771_Smartseq2). **D** Expression levels of *AEBP1* in the cell clusters in TME based on scRNA-seq data from TNBC (BRCA_GSE114727_inDrop). IF staining showed representative images of AEBP1 (green) and α-SMA (red) in human COAD (**E**) or TNBC (**F**) tissues. Scale bar, 50 μm. n = 3 biological replicates. Correlation between GZMB and AEBP1 expression in human COAD (**G**) or TNBC (**H**) samples was detected by IHC (two-sided Spearman correlation analysis). **I**, **J** Overall survival of COAD or TNBC patients with AEBP1^{high} or AEBP1^{low} expression levels in an in-house cohort. Source data are provided as a Source Data file.

Single-cell RNA sequencing revealed that AEBP1-educated CAFs inhibited T cell function

To further confirm the impact of AEBP1 in the TME, we profiled scRNA-seq analysis on EO771 tumors from WT and *Aebp1* cKO mice. In total, we identified 10 cell subsets based on classic cluster markers, including malignant cells, epithelial, monocytes, macrophages, T cells, natural killer (NK) cells, fibroblasts, neutrophil, endothelial and B cells (Supplementary Fig. 4A–C). Consistent with our above findings (Fig. 1C, D), *Aebp1* expression was notably enriched in the fibroblast population (Fig. 3A). Remarkably, lower numbers of pro-tumor cells, such as fibroblasts, macrophages, and neutrophils, were observed in the tumors of *Aebp1* cKO mice in comparison to those in WT mice (Fig. 3B). Conversely, increased levels of anti-tumor cells, specifically T cells and NK cells, were detected in the tumors of *Aebp1* cKO mice (Fig. 3B). To further explore the effect of *Aebp1* on mCAFs, we analyzed the fibroblast subtypes and identified four clusters: inflammatory CAFs (iCAF), extracellular CAFs (eCAF), antigen-presenting CAFs (apCAF), and myofibroblast CAFs (myCAF) (Supplementary Fig. 4D, E). The

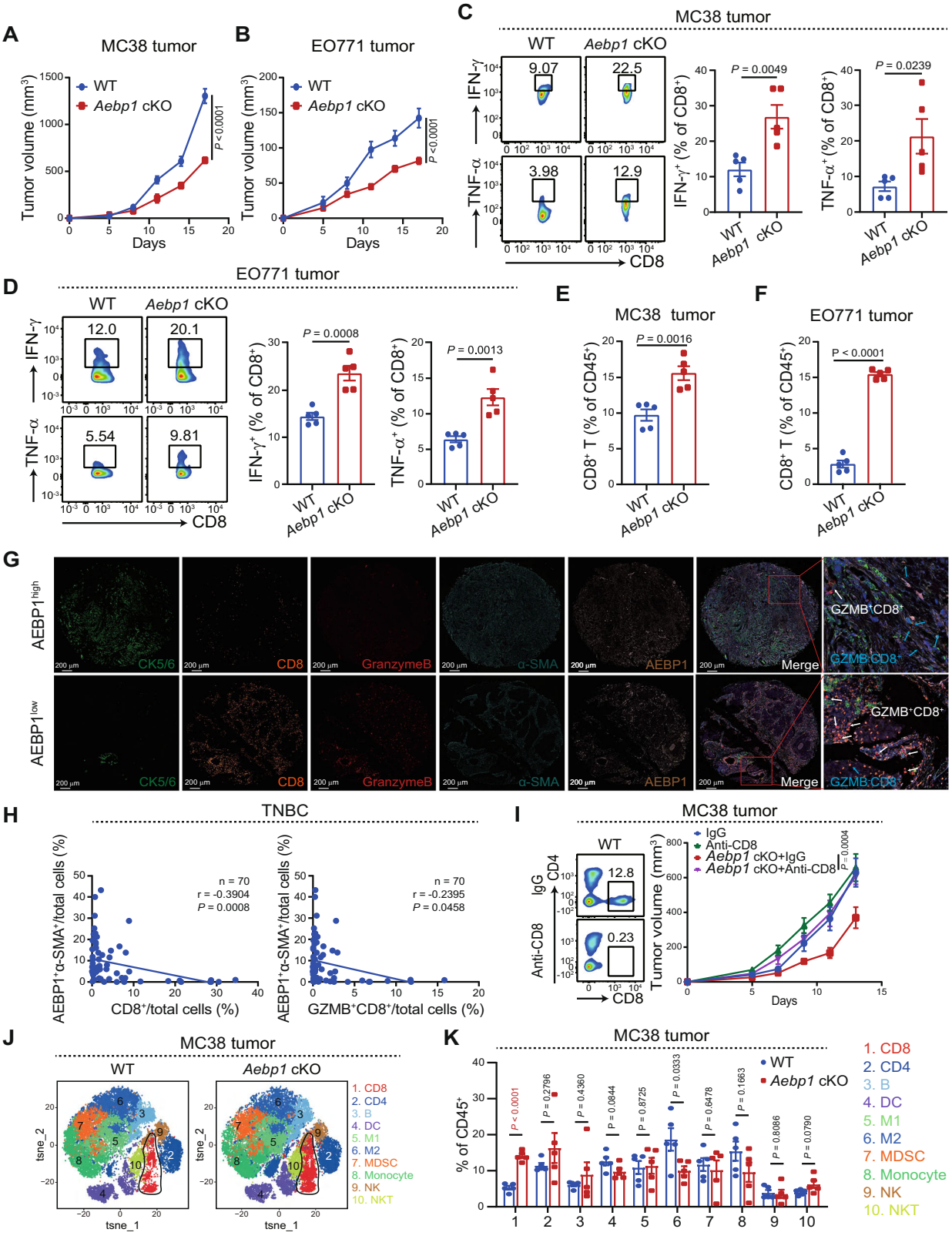

expression levels of *Aebp1* are elevated in iCAFs and apCAFs, while showing relatively lower expression in myCAFs (Supplementary Fig. 4F). Furthermore, our scRNA-seq revealed reduced fibroblast population in EO771 tumors of *Aebp1* cKO mice compared to WT control (Fig. 3B). This observation was corroborated by functional assays demonstrating significantly attenuated proliferation in *Aebp1*-deficient mCAFs relative to WT cells, coupled with diminished α-SMA immunoreactivity in *Aebp1* cKO tumors (Supplementary Fig. 4G, H). Notably, scRNA-seq analysis further showed a marked decrease in myCAF proportion and concomitant accumulation of iCAFs in *Aebp1*-deficient tumors (Fig. 3C). Intriguingly, *Aebp1* cKO-derived iCAFs exhibited enhanced secretion of chemokines *Cxcl9* and *Cxcl10* (Supplementary Fig. 4I). Our findings suggest that *Aebp1* might support myCAF-mediated stromal barrier formation to restrict $CD8^+$ T cell

Fig. 2 | Blocking *Aebp1* in fibroblasts enhances T cell antitumor immunity. MC38 (**A**) and EO771 (**B**) tumor growth from WT versus *Aebp1* cKO mice ($p < 0.0001$). Percentage of IFN-γ$^+$ and TNF-α$^+$ CD8$^+$ T cells in MC38 (**C**) and EO771 (**D**) tumors from WT versus *Aebp1* cKO mice. Percentage of CD8$^+$ T cells in MC38 (**E**) and EO771 (**F**) tumors from WT versus *Aebp1* cKO mice, $p < 0.0001$ (**F**). Representative images (**G**) and correlation between AEBP1$^+$α-SMA$^+$ cells and CD8$^+$ or GZMB$^+$CD8$^+$ T cells expression in human TNBC tissues (two-sided Spearman correlation analysis) (**H**). **I** MC38 tumor growth with CD8$^+$ T cells depleted by anti-CD8 antibodies. **J** tSNE plot of tumor infiltrating lymphocytes (TILs) overlaid with the expression of indicated markers from WT or *Aebp1* cKO group. **K** Frequency of clusters of indicated immune cell subsets in MC38 tumors from WT and *Aebp1* cKO group, $p < 0.0001$ for WT vs. cKO in cluster 1. n = 5 mice/group (**A**–**F**, **I**, **K**). Data are presented as the mean ± SEM (**A**–**F**, **I**, **K**). Data were analyzed by two-sided unpaired Student's t-test (**C**–**F**, **K**), and two-way ANOVA with Sidak's (**A**, **B**) or Tukey's (**I**) multiple comparisons test. Source data are provided as a Source Data file.

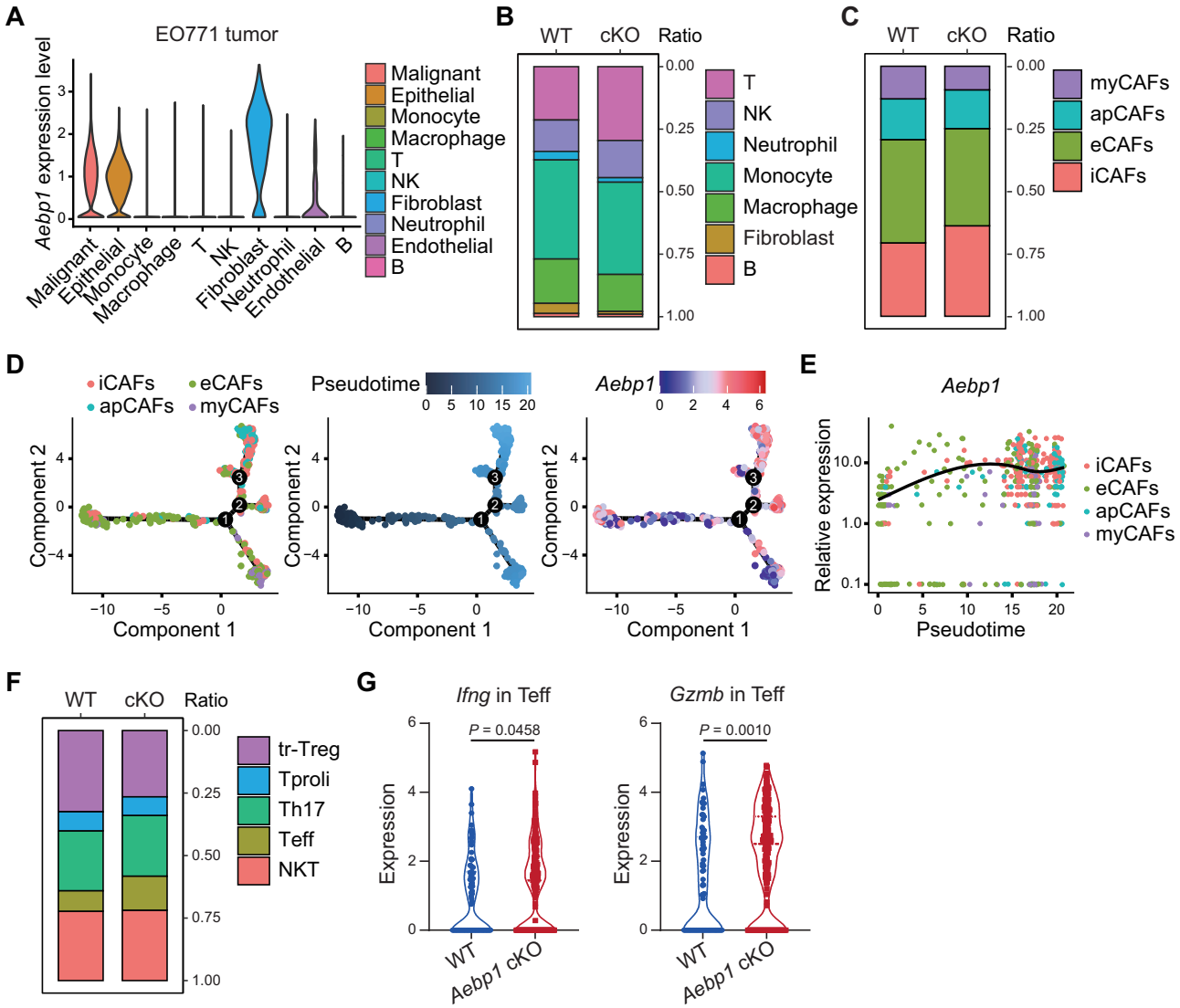

Fig. 3 | scRNA-seq uncovers that CAF-derived *Aebp1* reshapes the tumor immune microenvironment. A Expression level of *Aebp1* in the indicated cell clusters of EO771 tumors based on scRNA-seq. **B** Percentage of immune cell clusters in the EO771 tumors from WT or *Aebp1* cKO group. **C** Percentage of fibroblast subtypes in the EO771 tumors from WT or *Aebp1* cKO group. **D** Trajectory analysis of fibroblast subtypes. Cell types were color-coded and arranged by pseudo-time (left). Blue colors were based on pseudo-time (middle). Change of *Aebp1* expression in the cell types based on pseudotime (right). **E** The expression of *Aebp1* in indicated fibroblast subtypes based on pseudotime. **F** Percentage of indicated T cell clusters in the EO771 tumors from WT or *Aebp1* cKO group. **G** Expression levels of *Ifng* and *Gzmb* in the Teff cell clusters of EO771 tumors based on scRNA-seq analysis (n = 79 for WT, n = 191 for cKO, two-sided unpaired Student's t-test).

infiltration, while its ablation promotes chemokine-dependent T cell recruitment through iCAF activation.

To explore the potential impact of *Aebp1* on the CAFs origin in the tumorigenesis, we performed scRNA-seq trajectory analysis on the fibroblast subsets. The trajectory analysis showed the eCAFs cluster at the trajectory's start, myCAFs at the terminus of trajectory branch 1, iCAFs at the endpoint of trajectory branch 2, and apCAFs at the endpoint of trajectory branch 3 (Fig. 3D). Notably, eCAFs exhibited low *Aebp1* expression at the early trajectory stages, whereas elevated *Aebp1* expression was evident in apCAFs and iCAFs at later stages (Fig. 3D, E and Supplementary Fig. 4J). These findings support the notion that *Aebp1* derived from iCAFs or apCAFs could significantly contribute to tumor progression.

To further confirm the interaction between AEBP1-educated mCAFs and other cell clusters, we performed cell-cell communication analysis using scRNA-seq data. The interactions between CAFs and T

cells were diminished in TME of EO771 tumors from *Aebp1* cKO mice compared to WT mice (Supplementary Fig. 4K). To investigate how AEBP1-educated mCAFs affect T cells, we analyzed T cell subsets, identifying five main subsets: including tissue resident regulatory T cells (tr-Treg), proliferation T cells (Tproli), Th17, effector T cells (Teff) and NKT cells (Supplementary Fig. 4L, M). A lower number of tumor-infiltrating tr-Tregs and a higher number of Teff cells were observed in EO771 tumors derived from *Aebp1* cKO mice compared to those from WT mice (Fig. 3F). As expected, *Aebp1* loss significantly increased the production of cytokines, including *Ifng* and *Gzmb* (Fig. 3G). These data suggest that *Aebp1* deficiency significantly enhances the cytotoxic effect of T cells by inhibiting the interaction between CAFs and T cells.

Blocking AEBP1 down-regulates PD-L1 expression on CAFs

In order to further elucidate how AEBP1 in CAFs impairs antitumor immunity, we conducted a comparative analysis of global transcriptomic profiles between the control mCAFs and *Aebp1* knockdown mCAFs using RNA sequencing. Compared with control group, *Aebp1* knockdown mCAFs showed higher expression of genes associated with immune activation and T cell activation but lower expression of many genes related to immune suppression, indicating a regulatory role of *Aebp1* in mCAFs' immune function (Fig. 4A). Among the affected genes, PD-L1 (CD274), a crucial immune checkpoint protein implicated in CAF-mediated immune suppression[5], was notably downregulated in *Aebp1* knockdown mCAFs compared to controls (Fig. 4A). Consistent results were observed in the scRNA analysis of WT and *Aebp1*$^{-/-}$ mCAFs, highlighting a significant decrease in PD-L1 expression in *Aebp1*-deficient mCAFs (Fig. 4B). Additionally, spatial transcriptomic sequencing (stRNA-seq) of colon cancer samples demonstrated reduced PD-L1/PD-1 signaling in the AEBP1 low-expression group (Supplementary Fig. 5A). Moreover, the expression levels of AEBP1 and PD-L1 showed a positive correlation trend within the tumor stroma of human COAD and TNBC samples, as well as in mouse MC38 tumors (Fig. 4C and Supplementary Fig. 5B, C). This correlation was further supported by reduced PD-L1 expression in CAFs from MC38, EO771, and B16-F10 tumors in *Aebp1* cKO mice compared to WT mice (Fig. 4D, E and Supplementary Fig. 5D). Subsequent confirmation of downregulated PD-L1 expression in *AEBP1*-knockdown hCAFs, *Aebp1*$^{-/-}$ and *Aebp1*-knockdown mCAFs was conducted via real-time PCR and flow cytometry in vitro (Fig. 4F, G and Supplementary Fig. 5E, F). Additionally, the recombinant human or mouse AEBP1 (rhAEBP1/rmAEBP1) protein stimulated PD-L1 expression in both hCAFs and mCAFs (Fig. 4H, I and Supplementary Fig. 5G). By pre-treating WT hCAFs and mCAFs with a PD-L1-blocking antibody and then co-culturing them with T cells, levels of IFN-γ$^+$ and TNF-α$^+$ CD8$^+$ T cells were elevated to levels comparable to those co-cultured with *AEBP1*-knockdown hCAFs and *Aebp1*-deficient mCAFs, underscoring the role of PD-L1 as a key downstream mediator of pro-tumor immunity induced by AEBP1 (Fig. 4J and Supplementary Fig. 5H).

Given the secretory property of AEBP1 and the established contribution of tumor cell-intrinsic PD-L1 to immune evasion, we investigated AEBP1-mediated crosstalk between CAFs and malignant cells. Spatial transcriptomics profiling revealed lower PD-L1 in tumor cells from AEBP1^{low} versus AEBP1^{high} niches (Supplementary Fig. 5I). Consistently, tumor cells co-cultured with *Aebp1*$^{-/-}$ mCAFs showed reduced PD-L1 levels compared to WT controls, while supplementation with rmAEBP1 effectively induced PD-L1 expression in tumor cells (Supplementary Fig. 5J, K). Crucially, the regulatory effect of *Aebp1* on tumor PD-L1 (approximately 20% reduction upon knockout) proved substantially weaker than its autocrine control over CAF-intrinsic PD-L1 (nearly 50% reduction in *Aebp1*$^{-/-}$ mCAFs) (Fig. 4G), directing our focus to CAF-specific PD-L1 modulation.

CKAP4 is a receptor for AEBP1 activities in CAFs

To understand how AEBP1 regulates PD-L1 expression in CAFs, we conducted Kyoto Encyclopedia of Genes and Genomes (KEGG) signaling pathway enrichment analysis based on scRNA-seq data from WT and *Aebp1* cKO tumors. We found that the activity of the PI3K/Akt signaling pathway was most pronounced in fibroblasts (Fig. 5A and Supplementary Fig. 6A), which was also corroborated in KEGG analysis of mRNA-seq data from control mCAFs and *Aebp1*-knockdown mCAFs (Fig. 5B). We then confirmed that the activation of the PI3K/Akt signaling pathway was significantly suppressed in both *AEBP1*-knockdown hCAFs and *Aebp1*$^{-/-}$ and *Aebp1*-knockdown mCAFs, while recombinant AEBP1 notably activated this pathway in both hCAFs and mCAFs (Fig. 5C, D and Supplementary Fig. 6B). Consistent with previous findings (Supplementary Fig. 5J, K), AEBP1 also regulated PI3K/Akt signaling in tumor cells, though less prominently than in CAFs (Supplementary Fig. 6C). Since PI3K/Akt signaling axis is known to positively mediate PD-L1 expression[10], we interrogated the role of PI3K/Akt signaling pathway in AEBP1-regulated PD-L1 expression. We observed that PD-L1 in mCAFs was significantly down-regulated by a PI3K inhibitor LY294002 (Supplementary Fig. 6D). Furthermore, the Akt activator SC79 efficiently reversed the suppression of PD-L1 expression caused by *Aebp1* blockade (Fig. 5E). These findings suggest that PI3K/Akt signaling pathway is responsible for the function of AEBP1 in both hCAFs and mCAFs.

As AEBP1 can induce CAFs to generate immunosuppressive effects, we next evaluated whether a potential receptor for AEBP1 exists on the CAFs membrane. The proteins of mCAFs were extracted, immunoprecipitated with anti-AEBP1 antibody, and further analyzed by mass spectrometry (MS) (Supplementary Fig. 6E). Cytoskeleton-Associated Protein 4 (CKAP4), known to activate Akt signaling[11], emerged as one of the top proteins binding to AEBP1 (Supplementary Fig. 6F). This binding was validated through immunoblotting of the co-immunoprecipitate (co-IP) with an anti-AEBP1 antibody (Fig. 5F).

To further confirm whether AEBP1 colocalizes with CKAP4 on CAFs membrane, we incubated mCAFs with rmAEBP1 at 4°C for 3 hours. Confocal microscopy using fluorescence-labeled antibodies for AEBP1 and CKAP4 demonstrated that AEBP1 colocalizes with CKAP4 on the plasma membrane of mCAFs (Fig. 5G). shRNA-mediated knockdown of *Ckap4* expression in mCAFs efficiently abrogated AEBP1 localization on the cell surface, suggesting that AEBP1 interacts with CKAP4 at the plasma membrane of mCAFs (Fig. 5G). To map the CKAP4-interacting region, we generated four AEBP1 mutants based on structural domains annotated in UNIPROT (Fig. 5H). Co-IP assays demonstrated complete loss of CKAP4 binding in Mutant 1 compared to overexpressed WT AEBP1 (Fig. 5I). These results identified the Mutant 1 region as the primary CKAP4-binding domain essential for AEBP1. Moreover, the stRNA-seq analysis unveiled the concurrent expression of AEBP1 and CKAP4 in the TME (Supplementary Fig. 6G). ScRNA-seq analysis demonstrated that the expression of *Ckap4* was notably enriched in the fibroblast population, consistent with *Aebp1* (Supplementary Fig. 6H). Trajectory analysis of fibroblast subtypes revealed a parallel expression pattern between *Ckap4* and *Aebp1*. Specifically, low *Ckap4* expression was detected in the eCAFs at the initial stage, while high *Ckap4* expression was observed in the apCAFs and iCAFs at the later stages Supplementary Fig. 6I). To verify whether CKAP4 is a functional receptor for AEBP1, we examined whether silencing of CKAP4 influenced the biological effects of AEBP1 in CAFs. Indeed, shRNA-mediated knockdown of CKAP4 significantly suppressed Akt activation and PD-L1 expression induced by rhAEBP1/rmAEBP1 in both hCAFs and mCAFs (Fig. 5J, K and Supplementary Fig. 6J, K). Inhibiting *Ckap4* in mCAFs restored cytotoxic activities of CD8$^+$ T cells that were blocked by rmAEBP1-treated mCAFs (Fig. 5L, M). Collectively, these data suggest that AEBP1 could modulate PD-L1 expression by activating CKAP4/Akt pathway in CAFs.

Loss of *Aebp1* in CAFs enhances therapeutic responses to ICT

To investigate whether AEBP1 targeting could enhance immune checkpoint blockade (ICB) efficacy, we performed a retrospective

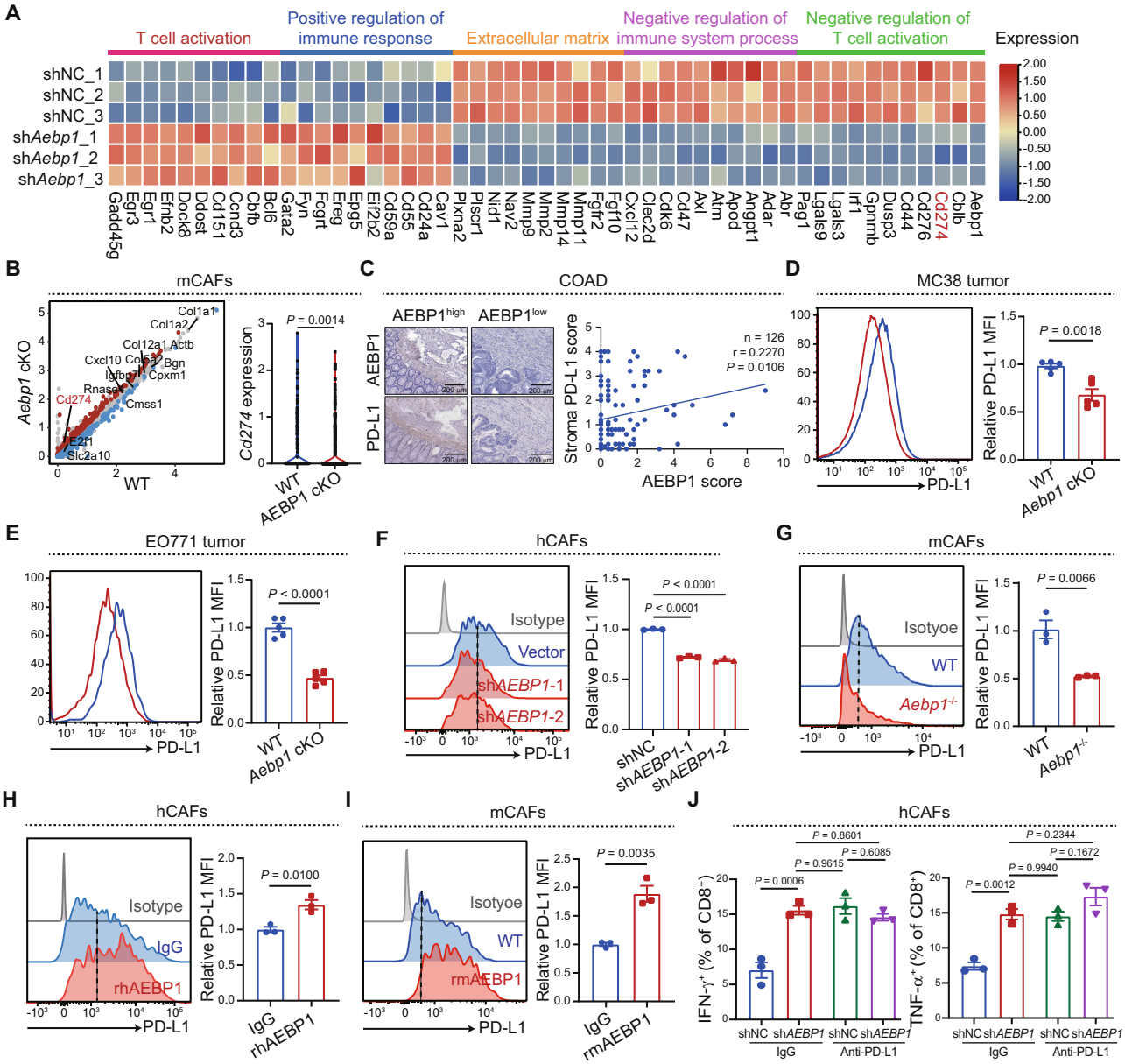

Fig. 4 | Blocking AEBP1 down-regulates PD-L1 expression on CAFs. A Gene ontology analysis by RNA sequencing of shNC or sh*Aebp1* mouse CAFs (mCAFs) (n = 3 mice/group). Heatmap shows the differentially expressed genes (DEGs) and associated signatures. **B** scRNA-seq analysis showing the expression of DEGs including *Cd274* in fibroblasts in EO771 tumors from WT (n = 184) or *Aebp1* cKO (n = 445) group. **C** The expression of PD-L1 in AEBP1^{high} or AEBP1^{low} human COAD samples was detected by IHC (two-sided Spearman correlation analysis). Flow cytometry analysis of PD-L1 expression on CAFs in WT or *Aebp1* cKO tumors of MC38 (**D**) and EO771 (**E**) models (n = 5 mice/group). Flow cytometry analysis of PD-L1 expression on shNC and *shAEBP1* hCAFs (**F**), or WT and *Aebp1*$^{-/-}$ mCAFs (**G**). Flow cytometry analysis of PD-L1 expression on hCAFs or mCAFs treated with IgG or rhAEBP1 (2 μg/ml) (**H**)/rmAEBP1 (1 μg/ml) (**I**). **J** Percentages of IFN-γ$^+$ or TNF-α$^+$ CD8$^+$ T cells co-cultured with shNC or *shAEBP1* hCAFs pre-treated with IgG, or anti-PD-L1 antibodies (10 μg/mL). n = 3 biological replicates (**F**–**J**). Data are presented as the mean ± SEM (**D**–**J**). Data were analyzed by two-sided unpaired Student's t-test (**B**, **D**, **E**, **G**–**I**), and one-way ANOVA with Dunnett's (**F**) or Tukey's (**J**) multiple comparisons test. $p < 0.0001$ (**E**, **F**). Source data are provided as a Source Data file.

biomarker analysis using the TIDE platform to evaluate correlations between AEBP1 expression and clinical outcomes in ICB-treated patients. Analyses revealed that elevated *AEBP1* expression significantly correlated with reduced survival in melanoma patients undergoing anti-CTLA-4 therapy (Supplementary Fig. 7A). Extending this observation to anti-PD-1-treated cohorts, we observed a similar trend toward poorer survival in both melanoma and glioblastoma patients with high *AEBP1* levels, though statistical significance was not achieved, potentially influenced by limited cohort sizes (Supplementary Fig. 7A). Based on these clinical insights, we further explored combinatorial strategies by integrating *Aebp1* targeting with anti-CTLA-4 therapy in the MC38 syngeneic model. Notably, *Aebp1* cKO mice receiving anti-CTLA-4 treatment showed the most effective tumor inhibition and dramatically prolonged survival (Fig. 6A), accompanied by increased CD8$^+$ T cell infiltration (Supplementary Fig. 7B), and more IFN-γ$^+$ and TNF-α$^+$ CD8$^+$ T cells compared to anti-CTLA-4-treated WT mice (Fig. 6B, C). Next, we examined whether inhibiting AEBP1 could also enhance therapeutic efficacy of anti-PD-1 treatment. Similarly, in EO771 model, AEBP1 inhibition plus anti-PD-1 combinatorial treatment achieved the highest therapeutic response compared with AEBP1 inhibition or ICT alone (Fig. 6D), along with enhanced T-cell function and infiltration (Fig. 6E, F and Supplementary Fig. 7C). Moreover, a

https://doi.org/10.1038/s41467-025-63659-w

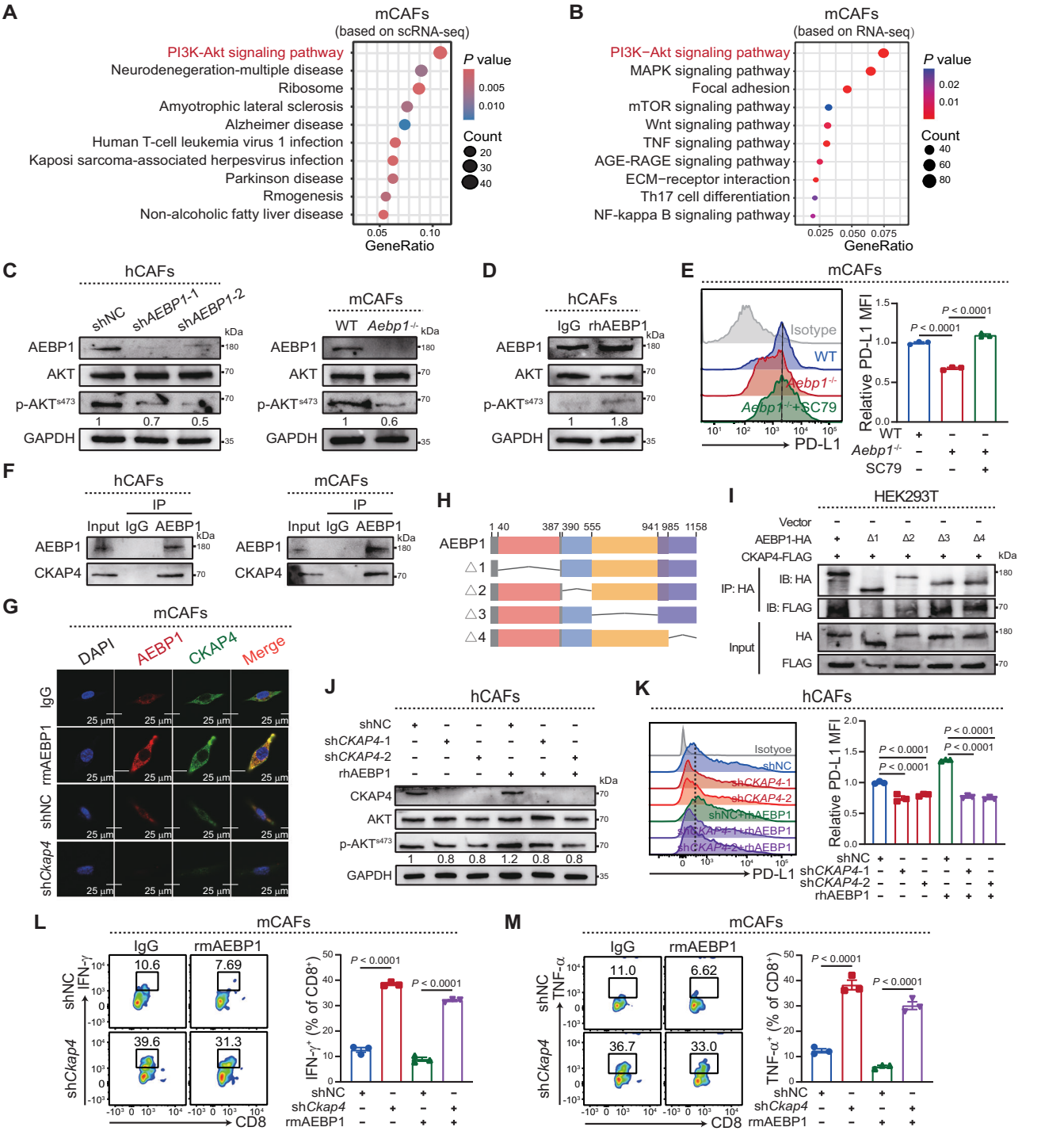

Fig. 5 | Ckap4 is a receptor for AEBP1 activities in CAFs. A KEGG analysis of scRNA-seq data showing the enriched signaling pathways in CAFs from WT tumors, in comparison to those from *Aebp1* cKO tumors. **B** KEGG analysis of RNA-seq data showing the enriched signaling pathways in shNC CAFs compared with sh*Aebp1* CAFs. Hypergeometric test (one-sided) with BH-FDR (**A**, **B**). **C** Western blot analysis of total AKT and p-AKT expression in shNC and sh*AEBP1* hCAFs, or WT and *Aebp1*$^{-/-}$ mCAFs. GAPDH was used as a loading control. **D** Western blot analysis of total AKT and p-AKT expression in hCAFs treated with IgG or rhAEBP1 (2 μg/ml). GAPDH was used as a loading control. **E** Flow cytometry analysis of PD-L1 expression on WT, *Aebp1*$^{-/-}$, or SC79 (20 μM) treated *Aebp1*$^{-/-}$ CAFs, $p < 0.0001$. **F** The binding status of AEBP1 and CKAP4 in hCAFs or mCAFs based on IP. **G** IF showed representative images of AEBP1 (red) and CKAP4 (green) in shNC and sh*Ckap4* mCAFs, or CAFs treated with IgG or rmAEBP1 (1 μg/ml). Scale bar, 25 μm. **H** Construction of AEBP1 serial deletion mutants. **I** IP and western blot were performed to analyze the co-expression of CKAP4 with either AEBP1 or its deletion mutants in 293 T cells. **J** Western blot analysis of total AKT and p-AKT expression in shNC or sh*CKAP4* hCAFs treated with vehicle or rhAEBP1 (2 μg/ml). GAPDH was used as a loading control. **K** Flow cytometry analysis of PD-L1 expression in shNC or sh*CKAP4* hCAFs treated with vehicle or rhAEBP1 (2 μg/ml), $p < 0.0001$. Percentage of IFN-γ$^+$ (**L**) or TNF-α$^+$ (**M**) CD8$^+$ T cells cocultured with shNC or sh*Ckap4* mCAFs treated with vehicle or rmAEBP1 (1 μg/ml), $p < 0.0001$. n = 3 biological replicates (**E**, **G**, **K**–**M**). Blot is representative of n = 2 biological replicates (**C**, **D**, **F**, **I**, **J**). Data are presented as the mean ± SEM, and were analyzed by one-way ANOVA with Tukey's multiple comparisons test (**E**, **K**–**M**). Source data are provided as a Source Data file.

https://doi.org/10.1038/s41467-025-63659-w

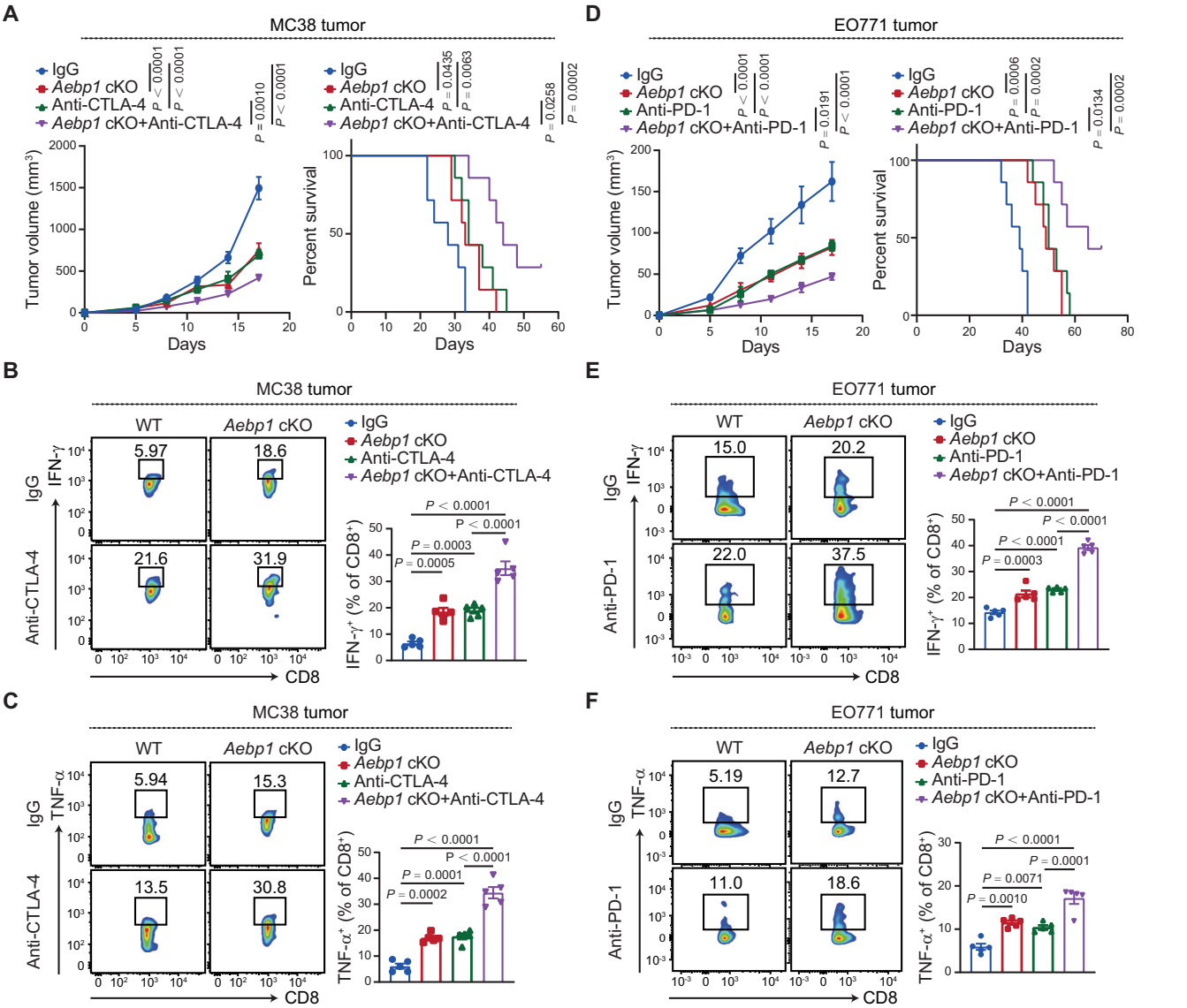

Fig. 6 | Depletion of AEBP1 in CAFs improves the efficacy of ICT. A MC38 tumor growth and survival analysis of IgG or anti-CTLA-4-treated WT and AEBP1 cKO mice. n = 5 mice/group for tumor volume analysis; n = 7 mice/group for survival analysis; log-rank test for survival comparison. Percentage of IFN-γ⁺ (**B**),TNF-α⁺ (**C**) CD8⁺ T cells in MC38 tumors from IgG, *Aebp1* cKO, anti-CTLA-4, and the combination groups (n = 5 mice/group). **D** EO771 tumor growth and survival analysis of IgG or anti-PD-1-treated WT and *Aebp1* cKO mice. n = 5 mice/group for tumor volume analysis; n = 7 mice/group for survival analysis; log-rank test for survival comparison. Percentage of IFN-γ⁺ (**E**),TNF-α⁺ (**F**) CD8⁺ T cells in EO771 tumors from IgG, *Aebp1* cKO, anti-PD-1, and the combination groups (n = 5 mice/group). Data are presented as the mean ± SEM (**A**–**F**), and were analyzed by two-way (**A**, **D**) or one-way ANOVA (**B**, **C**, **E**, **F**) with Tukey's multiple comparisons test. Source data are provided as a Source Data file.

significant decrease was observed in the population of TIM-3⁺ PD-1⁺ T cells in the combination therapy groups (Supplementary Fig. 7D–F). Together, AEBP1 blockade combined with ICT greatly improved the therapeutic response of multiple tumor models.

A small molecule inhibitor Chem-0199 targeting AEBP1 enhances antitumor immunity

To investigate AEBP1 more directly as a potential therapeutic target in cancer treatment, we explored the systemic inhibition of AEBP1 with a small molecule to potentially enhance antitumor immunity. Through a multi-step virtual screening process of compounds sourced from ChemDiv and ChemBridge, we identified series of small molecules as AEBP1 inhibitors (Fig. 7A). The top 5 candidate compounds with the highest docking scores to AEBP1's catalytic pocket were selected from each source and evaluated for their ability to inhibit AEBP1-CKAP4 binding activity using co-IP (Fig. 7B and Supplementary Fig. 8A, B). Following validation, ChemBridge-5340199 (hereafter referred to as Chem-0199) was chosen for further investigation based on its significant impact on inhibiting the interaction between AEBP1 and CKAP4 in CAFs (Fig. 7C and Supplementary Fig. 8B, C).

We next checked whether Chem-0199 could exert biological effect via AEBP1/CKAP4 pathway in CAFs. Chem-0199 dose-dependently suppressed the activation of Akt pathway and PD-L1 expression in CAFs (Supplementary Fig. 8D, E). Remarkably, Chem-0199 treatment of *Aebp1*$^{-/-}$ CAFs didn't further inhibit Akt activation, PD-L1 expression and CAF-mediated T-cell dysfunction compared to vehicle-treated *Aebp1*$^{-/-}$ CAFs (Fig. 7D–F and Supplementary Fig. 8F), suggesting that the in vitro effects of Chem-0199 on CAFs was mediated by AEBP1. We then assessed the antitumor activity of Chem-0199 in vivo. Intraperitoneal administration of Chem-0199 dose-dependently reduced the size of MC38 tumors compared to the vehicle group (Supplementary Fig. 8G). To test whether the direct effect of Chem-0199 on tumor cells

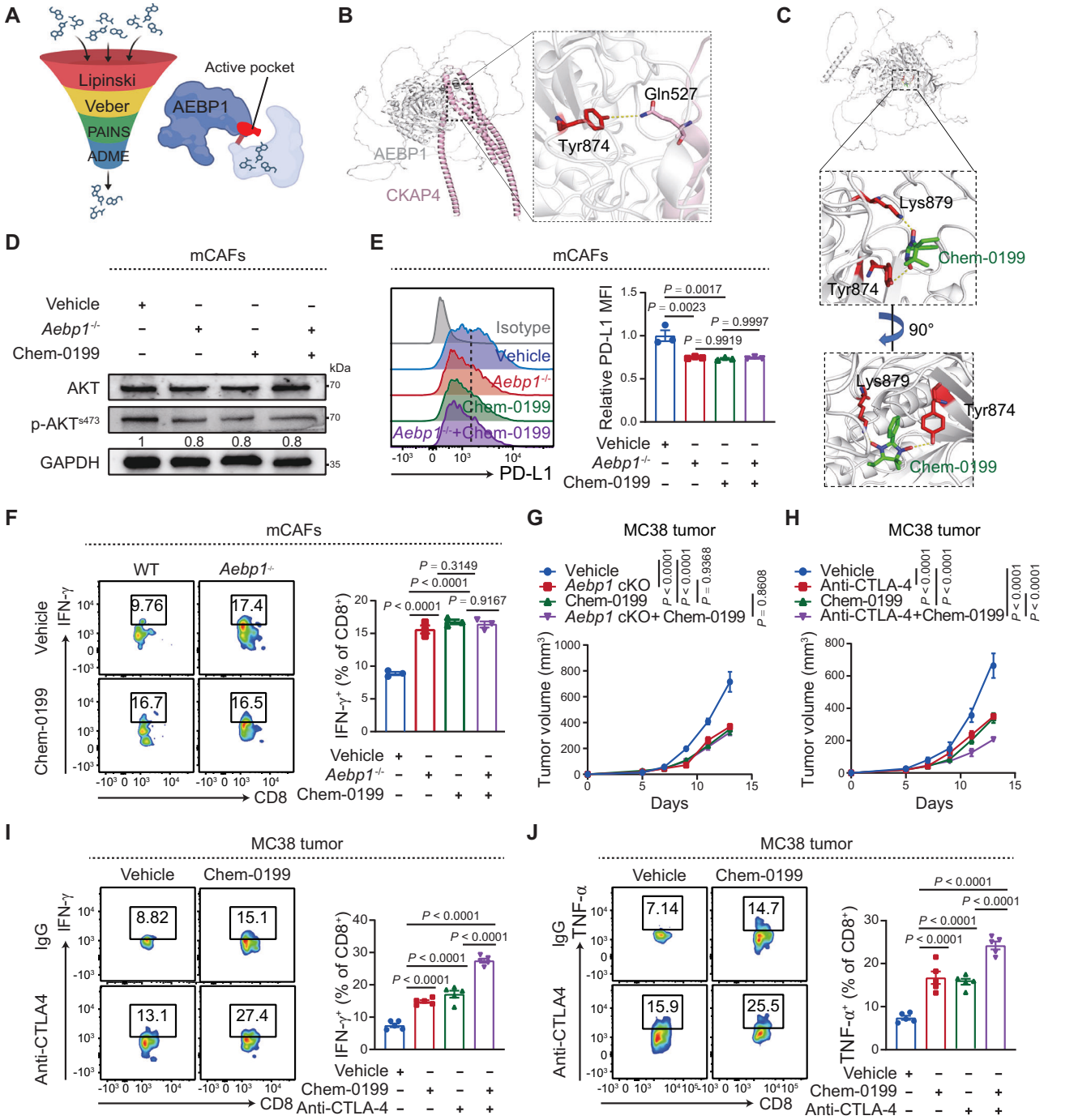

Fig. 7 | Chem-0199 suppresses the interaction between AEBP1 and CKAP4. **A** Workflow of inhibitor screening. Created in BioRender. Xiaoyu, W. (2025) https://BioRender.com/s97i4nk. **B** Overall structures of AEBP1 (shown in silver) and CKAP4 (shown in pink). The figure demonstrates the formation of a hydrogen bond (represented by yellow dashed lines) between the amino acid Tyr874 in the AEBP1 protein and the amino acid Gln527 in the CKAP4 protein. **C** Close-up views of AEBP1-Chem-0199 complexes. The figure illustrates the competitive binding of Chem-0199 to AEBP1, forming hydrogen bonds and π-π interactions specifically with the amino acid Tyr874 in the AEBP1 protein. The green arrows indicate Chem-0199. Two perpendicular views are shown. **D** Western blot analysis of total AKT and p-AKT expression in vehicle or Chem-0199 treated WT and *Aebp1*$^{-/-}$ CAFs. GAPDH was used as a loading control. Blot is representative of n = 2 biological replicates. **E** Flow cytometry analysis of PD-L1 expression on vehicle or Chem-0199 treated WT and *Aebp1*$^{-/-}$ mCAFs. **F** Percentage of IFN-γ$^+$ CD8$^+$ T cells cocultured with WT and *Aebp1*$^{-/-}$ mCAFs treated with vehicle or Chem-0199. **G** MC38 tumor growth of vehicle or Chem-0199-treated WT and *Aebp1* cKO mice. **H** Tumor growth of MC38 tumor-bearing WT mice treated with Chem-0199 alone, anti-CTLA-4 alone, or Chem-0199 + anti-CTLA-4. Percentage of IFN-γ$^+$ (**I**) or TNF-α$^+$ (**J**) CD8$^+$ T cells in MC38 tumors from mice treated with indicated regimens, $p < 0.0001$. n = 3 biological replicates (**E**, **F**), n = 5 mice/group (**G**–**J**). Data are presented as the mean ± SEM (**E**–**J**), and were analyzed by one-way (**E**, **F**, **I**, **J**) or two-way ANOVA (**G**, **H**) with Tukey's multiple comparisons test. Source data are provided as a Source Data file.

contributes to its inhibition on tumor growth in vitro, we treated multiple tumor cells with Chem-0199 and observed similar proliferation rates (Supplementary Fig. 9A–C), suggesting that the attenuation of tumor growth by Chem-0199 in mice was unlikely to result from direct suppression of Chem-0199 on tumor cells. To be noted, the inhibition of tumor growth by Chem-0199 could not be further improved in *Aebp1* cKO mice, indicating that the suppression of tumor growth by Chem-0199 might be attributable to AEBP1 inhibition in

CAFs (Fig. 7G). Then, we determined whether the response to Chem-0199 might be enhanced further by ICT. Similar to experiments using genetic KO of *Aebp1* in CAFs, Chem-0199 plus anti-CTLA-4 exhibited significantly superior efficacy in inhibiting MC38 tumor growth compared to Chem-0199 or ICT treatment alone (Fig. 7H). Furthermore, we examined the effect of Chem-0199 on tumor immunity. The population of IFN-γ$^+$ and TNF-α$^+$ CD8$^+$ T cells were markedly higher in tumor sections from the Chem-0199 treatment group than in the control group (Fig. 7I, J). Importantly, the combination of Chem-0199 and ICT substantially boosted the cytotoxic activity of T cells compared to individual treatment (Fig. 7I, J).

Considering that adverse effects may lead to intolerance in treatment procedures and negatively impact its clinical efficacy, we next evaluated the in vivo toxicity of Chem-0199 in mouse models. Complete blood count (CBC) results showed no marked discrepancies in white blood cells (WBC), red blood cells (RBC), hemoglobin (Hb), and platelets (PLT) between the control group and the Chem-0199 treatment group (Supplementary Fig. 9D). Hematoxylin-eosin (H&E) staining indicated that Chem-0199 exhibited no significant toxicity to the heart, liver, lung, kidney, and intestine tissues in mice (Supplementary Fig. 9E).

Discussion

CAFs are a type of crucial stromal cells present in the TME, playing indispensable roles in promoting tumor growth, progression, and therapeutic resistance[12]. Increasing studies have indicated that CAFs can promote tumor immune escape by releasing cytokines, expressing immune checkpoint molecules, and remodeling the ECM, although the detailed molecular mechanisms require further clarification[13–15]. While previous investigations have established AEBP1's role in driving fibroblast activation and its inverse correlation with CD8$^+$ T cell infiltration, its precise immunomodulatory mechanisms within the TME remain undefined[16,17]. This study elucidates AEBP1 as a central upstream regulator controlling CAF-mediated immunosuppression. We demonstrate that AEBP1 induces CD8$^+$ T cell dysfunction by upregulates PD-L1 expression, a critical immune checkpoint molecule on CAFs. Concurrently, we found that AEBP1 expression in CAFs restricts T cell infiltration into the TME. By collectively suppressing T cell function and abundance, AEBP1 impairs anti-tumor immunity and significantly contributes to tumor immune evasion.

In the TME, CAFs demonstrate significant heterogeneity and can be classified into different subtypes based on their phenotypic characteristics and functions[18]. Among them, myCAFs express high levels of α-SMA, while eCAFs exhibit high expression of ECM proteins such as collagen and fibronectin, both participating in ECM remodeling to enhance tumor cell migration and invasion abilities[19,20]. In contrast, iCAFs display an inflammatory phenotype and can influence tumor progression by secreting cytokines and chemokines[21]. Additionally, apCAFs are a unique subtype expressing major histocompatibility complex (MHC) class II molecules, capable of presenting antigens to T cells to regulate immune responses within the TME, potentially either promoting or suppressing antitumor immunity[22]. A positive correlation was observed between elevated levels of iCAFs and improved prognosis, while increased levels of myCAFs were associated with a poorer prognosis[23]. Our study here revealed that inhibiting AEBP1 significantly increased the proportion of iCAFs and decreased the proportion of myCAFs within CAF populations. Furthermore, *Aebp1* exhibited higher expression levels in iCAFs and apCAFs, which are closely associated with tumor immunity, suggesting the potential important role of *Aebp1* in modulating CAF immune functions. Critically, *Aebp1* inhibition fosters an iCAF-enriched microenvironment that amplifies *Cxcl*9/10 secretion, chemokines critical for cytotoxic T cell recruitment and macrophage polarization regulation[24,25]. Consistent with this mechanism, CyTOF analysis revealed reduced M2-like macrophage infiltration upon *Aebp1* suppression, a phenomenon potentially driven by elevated *Cxcl*9/10. Collectively, these findings position AEBP1 as a modulator of the tumor immunosuppressive microenvironment through CAF-dependent pathways, though mechanistic details await further elucidation.

PD-L1 plays a crucial role in the tumor immune microenvironment. Tumor cells and various immune cells in the TME, including macrophages, dendritic cells, and B cells, inhibit antitumor immunity by expressing PD-L1[26]. Accumulating studies have shown significant expression of PD-L1 in CAFs, implicating their participation in tumor immune evasion, although the regulatory mechanisms remain unclear[13,27]. Our findings unveiled AEBP1 as a vital upstream regulator of PD-L1 expression in CAFs. PD-L1 expression is regulated by signaling pathways such as JAK/STAT, NF-κB, and PI3K/Akt[28]. Our study revealed that AEBP1 upregulates PD-L1 expression by activating the PI3K/Akt signaling pathway, highlighting the crucial role of PI3K/Akt signal pathway in promoting tumor progression mediated by CAFs. Furthermore, our study confirmed that CKAP4 is a key receptor for AEBP1 in CAFs, mediating the activation of the PI3K/Akt signaling pathway. CKAP4 was shown to interact with various signaling pathways, including Wnt, PI3K/Akt, and MAPK, influencing the biological behavior of tumor cells[11,29]. Increased CKAP4 expression was associated with aberrant tumor cell proliferation, hastening tumor progression and metastasis[30,31]. Notably, while CKAP4 demonstrates broad expression across multiple TME components, our analyses identify CAFs as showing the highest *Ckap4* expression levels. Furthermore, despite CAF-derived AEBP1 exhibiting weak paracrine control over tumor cell Akt/PD-L1, its CAF-intrinsic autocrine signaling dominates functional output. This CAF-restricted hierarchy positions CAFs as central coordinators of the AEBP1/CKAP4 axis.

Contrasting previous tumor cell-centric models of AEBP1 in malignancy[9,32,33,34], we unveil its CAF-selective operational mode. Systematic comparisons revealed predominant AEBP1/CKAP4 co-enrichment in CAFs rather than tumor cells. CAF-specific AEBP1 suppression failed to alter tumor cell proliferation or metastasis in vitro or immunocompromised hosts, yet immunocompetent models coupled with CD8$^+$ T cell depletion revealed its essential immunosuppressive role. These results recalibrate understanding of the AEBP1/CKAP4 axis, positioning CAF-specific expression as the linchpin of its TME-modulatory function.

ICT has demonstrated promising potential in cancer treatment, yet its efficacy remains limited to a subset of patients, underscoring the need for enhanced strategies[35]. Our study demonstrates that AEBP1 inhibition synergizes with both anti-CTLA-4 and anti-PD-1 therapies through complementary mechanisms, despite their distinct cellular targets. For the observed synergy with anti-PD-1, while PD-L1 regulation in CAFs constitutes a primary pathway, AEBP1 also exerts broader immunosuppressive effects by driving CAF proliferation and remodeling the tumor microenvironment. These coordinated modifications amplify anti-PD-1 efficacy through spatial synergy: neutralizing PD-L1 on tumor/myeloid cells with ICB while simultaneously targeting CAF-mediated PD-L1 regulation and stromal immunosuppression via AEBP1 inhibition. This multilayered intervention across distinct cellular compartments enhances immune activation, underscoring AEBP1's potential as a combinatorial immunotherapy target. Additionally, our study identified Chem-0199, a small molecule inhibitor targeting the AEBP1/CKAP4 pathway, which effectively inhibited tumor growth and enhanced ICT efficacy without substantial adverse effects. Further investigation is warranted to determine the clinical translational value of this compound.

In summary, our study revealed that CAF-derived AEBP1 binds to the downstream ligand CKAP4 in an autocrine manner, triggering the activation of the PI3K/Akt pathway and the upregulation of PD-L1 on CAFs, thereby resulting in T cell dysfunction. Genetic or pharmaceutic inhibition of AEBP1 in CAFs restrains tumor progression and enhances the efficacy of immunotherapy (Fig. 8). These findings highlight the crucial role of AEBP1 in CAF-mediated tumor immune evasion and

https://doi.org/10.1038/s41467-025-63659-w

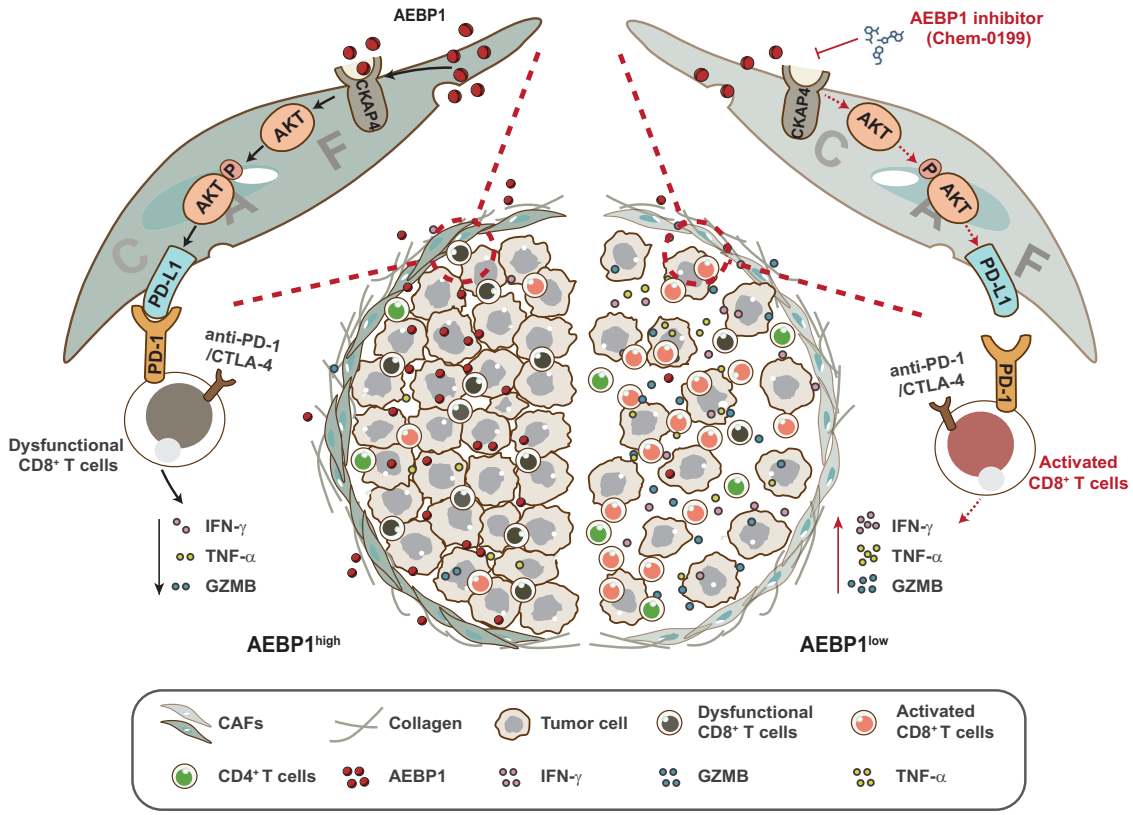

Fig. 8 | Schematic illustration of the mechanism by which CAF-derived AEBP1 induces T cell dysfunction in tumors. CAF-derived AEBP1 activates the CKAP4/AKT/PD-L1 pathway, then leads to T cell dysfunction. Chem-0199, an AEBP1 inhibitor, disrupts the AEBP1-CKAP4 complex, suppresses the activation of Akt pathway and PD-L1 expression in CAFs, and finally enhances the cytotoxic activity of $CD8^+$ T cells. Furthermore, genetic or pharmaceutical inhibition of AEBP1 synergizes with ICT.

demonstrates its potential as a diagnostic biomarker and therapeutic target in cancer treatment.

Methods

Cell culture

Murine colorectal carcinoma cell lines MC38 (3101MOUTCM46) was sourced from National Infrastructure of Cell Line Resource (NICR, Beijing, China). Murine colorectal carcinoma cell lines CT26 (CRL-2638), murine mammary carcinoma cell lines EO771 (CRL-3461), EMT6 (CRL-2755), and 4T1 (CRL-2539), human mammary cell line MDA-MB-231 (HTB-26), the melanoma cell line B16-F10 (CRL-6475), and human embryonic kidney cell line 293 T (CRL-3216) were all sourced from the American Type Culture Collection (ATCC). The mCAFs were isolated from the EO771/MC38 tumors and hCAFs were isolated from human breast cancer tissues. The cells were consistently cultured at 37 °C with 5% CO_2, with the medium being refreshed daily. Treatments comprised recombinant mouse AEBP1 (1 μg/mL; Abcam, ab225975), human AEBP1 (2 μg/mL; R&D, 6425-AC), LY294002 (T2008), and SC79 (T2274) (20 μM each; TargetMol).

RNA sequencing analysis

COAD and TNBC tumor tissues were subjected to RNA extraction employing Trizol reagent (15596026, Invitrogen). The RNA samples were then prepared for sequencing at ANNOROAD, where they underwent library construction and were sequenced using the Nova-Seq platform. The resulting FASTQ files from RNA-Seq were analyzed with htseq to determine gene read counts, which were then converted to TPM values. Subsequently, principal component analysis (PCA) was conducted using R software. The GSVA package was downloaded from http://www.bioconductor.org. GSEA analysis was performed utilizing the Java Web Start platform. To identify differentially expressed genes, an analysis was conducted using the R statistical package DESeq2 (version 1.42.0). The thresholds for significance were set to a fold change > 2, an adjusted p value < 0.05, and the mean $\log_2$ expression level for the high expression group exceeding 0.

Identification of genes associated with T cell dysfunction

To identify genes correlated with T cell dysfunction, we first established a T cell activation signature comprising key immunoregulatory markers (RAB27A, IL12A, XCL1, IFNG, PRF1, GZMB, CCL5, TBX21, CD8A, GZMA, IL2, PTPRC, ICOS, GZMM, GNLY)[36,37], followed by GSVA scoring of samples. Cohort stratification into T cell activation (high-score) and dysfunction (low-score) groups was performed using median GSVA values as the threshold.

Human samples

Tumor tissues from patients diagnosed with COAD and TNBC were procured from the First Affiliated Hospital of Chongqing Medical University. The acquisition of pathological samples and the examination of pertinent patient medical records received approval from the Research Ethics Committee of the First Affiliated Hospital of Chongqing Medical University (Project Approval No. 2022-K121). All participants or their legal representatives provided written informed consent as necessary.

IF and IHC staining

For IF, sections were blocked with goat serum for 20 minutes, incubated with primary antibodies at 4 °C overnight, followed by incubation with appropriate fluorescent secondary antibodies. Nuclei were counterstained with DAPI during mounting. Images were captured

using a LEICA (DMI4000B) microscope. For IHC, endogenous peroxidase was blocked with 3% H_2O_2, followed by blocking with goat serum for 20 minutes. Sections were incubated with primary antibodies at 4 °C overnight, followed sequentially by a biotinylated secondary antibody and horseradish peroxidase-conjugated streptavidin. Color development was achieved using 3,3′-Diaminobenzidine (DAB), followed by hematoxylin counterstaining, dehydration, and mounting. Slides were scanned for analysis.

For IF staining, the primary antibodies employed encompassed anti-α-SMA (ab7817, Abcam, 1:100) and anti-AEBP1 (ab254973, Abcam, 1:100). In IHC staining, anti-AEBP1 (ab254973, Abcam, 1:200; sc-271374, Santa, 1:100), anti-CD8a (ab199016, Abcam, 1:200; 98941, CST, 1:200), anti-GZMB (ab4059, Abcam, 1:100; 44153, CST, 1:50), and anti-PD-L1 (66248-1-Ig, Proteintech, 1:5000) were applied. Secondary antibodies conjugated with DyLight 488 or DyLight 594, targeting mouse or rabbit IgG were sourced from Thermo Fisher Scientific.

The TNBC tissue microarray (AF-BrcSur2202) was constructed and multiplex immunofluorescence staining was performed by Hunan Aifang Biotechnology Co., Ltd (China). For each sample, five randomly selected fields of view were used to count the number of target cells, with the help of HALP software (India Labs).

In our IHC analysis, AEBP1 expression was quantified using a standardized scoring system evaluating both staining intensity (0 = negative, 1 = pale yellow, 2 = brown-yellow, 3 = dark brown) and percentage of positive cells (0 = 0-5%, 1 = 6-25%, 2 = 26-50%, 3 = 51-75%, 4 = > 75%), with the final score calculated as the average of (intensity × percentage) across five representative high-power fields (400×). PD-L1 expression was assessed by averaging the percentage of positive cells across five fields. Similarly, $GZMB^+$ and $CD8^+$ cell counts were determined by averaging counts from five specified fields (400×/200×). All scoring was performed independently by the pathologist.

Gene modulation by lentiviral transduction and plasmid transfection

Lentiviral particles for human or mouse AEBP1-targeting shRNAs, mouse CKAP4-targeting shRNAs were sourced from Genecopoeia. The lentiviral expression vector was co-transfected with lentivirus packaging vectors into 293 T cells using the Lipofectamine™ 2000 (11668019, Invitrogen). Subsequently, CAFs were stably transfected with viral particles for 48-72 hours.

Human AEBP1 (with 3× HA tag), four AEBP1 mutants (with 3× HA tag), and human CKAP4 (with 3× FLAG tag) overexpression (OE) plasmids were obtained from Genecopoeia. These plasmids were expressed in 293 T cells using Lipofectamine™3000 (ThermoFisher) for transfection. 293 T cells were sequentially transfected with HA-tagged AEBP1 (OE/mutants) and FLAG-tagged CKAP4 (24 h interval; total 60-72 h). Mutants were designed using Uniprot domain mapping.

Animals

We procured 6 to 8-week-old C57BL/6-background *Aebp1*$^{flox/flox}$ mice (S-CKO-17395) from The Cyagen Biosciences, and S100A4^{CreERT} mice (NM-KI-200024) from Shanghai Model Organisms Center, Inc. Wildtype (WT) C57BL/6 (stock number: N-0005), WT BALB/c mice (stock number: N-0004) and BALB/c nude mice (stock number: N-0007) were sourced from Ensiweier (Chongqing, China). The *Aebp1*$^{flox/flox}$ mice were mated with *S100a4*^{CreERT} mice to create *Aebp1*$^{flox/flox}$*S100a4*^{CreERT} mice. Prior to tumor cell inoculation, these mice received intragastric administration of tamoxifen (T5648, 60 mg/kg, Sigma-Aldrich) over five consecutive days. Compliance with the laboratory animal care and use guidelines was strictly maintained throughout all experimental processes, and the protocols were vetted and endorsed by the Institutional Animal Care and Use Committee of Chongqing Medical University (IACUC-CQMU-20210222). The mice were housed in a specific pathogen-free (SPF) animal facility, with experimental and control animals housed separately. The housing conditions were maintained at a stable temperature of 21-23 °C, humidity levels within the range of 40-60%, and a 12-hour light/dark cycle. Carbon dioxide euthanasia was performed immediately when the longest diameter of the tumor in their bodies reaches 20 mm or the tumor volume reaches 2000 mm^3. The maximum tumor burden permitted by our institutional animal care protocol was not exceeded.

Tumor models

MC38 cells and CT26 cells (1.0×10^5 cells), along with B16-F10 cells (1.5×10^5 cells), were implanted subcutaneously into the proximal region of the mice's right hind legs. In the mammary tumor model, 4T1 cells, EMT6, and EO771 (1.0×10^5 cells) cells were implanted into the mammary fat pad of WT BALB/c, *Aebp1*$^{flox/flox}$, or *Aebp1*$^{flox/flox}$*S100a4*^{CreERT} C57BL/6 mice. Both male and female C57BL/6 and BALB/c mice were used for colon cancer models (MC38, CT26), and melanoma model (B16-F10), and female C57BL/6 and BALB/c mice were used for breast cancer models (4T1, EMT6, EO771). Before tumor formation, mCAFs were mixed with CT26, 4T1, or EMT6 cells at a ratio of 3:1. Tumor size estimation utilized the formula: volume (mm^3) = (long axis) × (short axis)^2/2. Anti-PD-1 antibody (RMP1-14, 10 mg/kg, Bioxcell) and anti-CTLA-4 antibody (9D9, 5 mg/kg, Bioxcell) were intraperitoneally administered on days 5, 7, 9, 11, and 13 post-tumor inoculation. In cases of in vivo $CD8^+$ T cell depletion, the mice received treatment with anti-CD8 antibody (YTS 169.4, 10 mg/kg, Bioxcell) every 3 days, beginning 3 days before MC38 tumor inoculation. The depletion efficacy of $CD8^+$ T cell was confirmed through flow cytometry analysis.

Cell isolation

Tumor samples were initially mechanically dissociated using a scissor device, followed by enzymatic digestion with Liberase (5401119001, 2 mg/mL, Roche) in DMEM at 37 °C for 30 minutes to create a homogenate. Subsequently, the homogenate was sieved through a 70 μm filter (bs-70-xbs, BioSharp) to isolate a single cell suspension, which was then treated with red blood cell lysis buffer for 2 minutes, washed, and resuspended in flow cytometry buffer for subsequent analysis. For CAF isolation, after red blood cell lysis, cells were resuspended in complete medium and plated in culture dishes. Following 15-min incubation at 37 °C, non-adherent cells were discarded. The adherent fraction, enriched for stromal cells including CAFs, was expanded in culture. Secondary purification of CAFs was achieved via morphological selection and immunophenotypic validation. Following the generation of a single cell suspension from the tumor specimens utilizing the aforementioned procedure, cells were cultured in Dulbecco's Modified Eagle Medium (DMEM, 11965092, Gibco), enriched with a 10% concentration of fetal bovine serum (04-001-1Acs, BI) and an additional 1% penicillin-streptomycin (15140122, Gbico) mixture. CAFs were identified as cells adhering to the culture vessel within 15 minutes, whereas non-adherent cells were discarded.

Flow cytometry analysis

Using the Fixable Viability Dye eFluor 450 (65-0863-14, Invitrogen, 1:1000), live cells were stained at 4 °C for 30 minutes to identify viable cells. Cells were pre-treated with anti-CD16/32 (101302, BioLegend) to block Fc receptors, followed by a 10-minute incubation on ice. Following washing, cells were incubated with a combination of primary antibodies against various cell surface markers. For mouse markers: CD45 (30-F11), CD4 (GK1.5), CD8a (53-6.7), CD11b (M1/70), CD140a (APA5), PD-L1 (10 F.9G2), Tim-3 (B8.2C12), PD-1 (MH5A); for human markers: CD45 (2D1), CD8a (SK1), CD11b (M1/70), PD-L1 (29E.2A3); all sourced from BioLegend. After stimulating cells with the Cell Stimulation Cocktail (00-4975-93, Invitrogen) at 37 °C for 4-6 hours, cytokines were stained with anti-IFN-γ (XMG1.2-mouse, 4S.B3-human, BioLegend) and anti-TNF-α (MP6-XT22-mouse, MAb11-human, BioLegend) antibodies. All antibodies were diluted at a ratio of 1:100 unless otherwise specified. Stained cells were analyzed using the BD

FACSCanto II Flow Cytometer and BD FACSDiva software (BD Biosciences), with data processed using FlowJo software (version 10.5.3).

CyTOF analysis

As previously mentioned, individual live cells were extracted from tumor tissues for CyTOF analysis. The cells underwent a viability assessment using cisplatin (HY-17394, 25 μM, MedChemExpress) for 1 minute, followed by labeling with a metal-tagged cocktail of monoclonal antibodies targeting cell surface molecules. After fixation and permeabilization with Buffer (88-8824-00, eBioscience), cells were labeled with a panel of monoclonal antibodies targeting intracellular antigens. Analysis was performed on the CyTOF 2 platform at the Liver Disease Institute, Beijing You'an Hospital. The data files generated were standardized and processed with Cytobank (version 9.1). Data were transformed using the cytofAsinh method before Phenograph clustering analysis, performed with the R cytofkit package version 0.99.0, for categorizing immune subsets from consolidated samples. The heatmaps depicted the mean intensity for markers across distinct clusters, where the frequency of cells within a cluster was determined by the ratio of the count of identified cells to the overall count of $CD45^+$ cells within the identical specimen. For the mass cytometry procedure, antibodies from Fluidigm were employed, encompassing a range of markers including anti-NK1.1 (142Ce), anti-CD40 (160Dy), anti-KI67 (161Dy), anti-TIM3 (162Dy), anti-LY6C (163Dy), anti-CD68 (164Dy), anti-GATA3 (167Er), anti-CD8 (168Er), anti-CD103 (151Eu), anti-CD69 (153Eu), anti-LY6G (152Gd), anti-CTLA4 (154Gd), anti-TIGIT (155Gd), anti-CD14 (156Gd), anti-LAG3 (158Gd), anti-FOXP3 (165Ho), anti-MHCII (175Lu), anti-B220 (176Lu), anti-CD11B (143Nd), anti-SIGLECF (144Nd), anti-CD4 (145Nd), anti-CD127 (141Pr), anti-CD25 (147Sm), anti-TBET (148Sm), anti-CD19 (149Sm), anti-CD11C (150Sm), anti-F4/80 (159Tb), anti-CD206 (169 T), anti-CD45 (89Y), anti-CD80 (171Yb), anti-CD86 (172Yb), anti-PD1 (173Yb), and anti-CD3 (174Yb).

Single cell RNA sequencing

Single-cell suspensions of EO771 tumors were obtained from WT or *Aebp1* cKO mice. Samples of three tumors from the same cohort were amalgamated at random to form a composite sample, which was then shipped to Beijing Annoroad (ANNOROAD) for sequencing. Subsequent to cell quantification, the samples were processed and sequenced on the Illumina NovaSeq 6000 platform in San Diego, California, following the manufacturer's protocol. Demultiplexing, barcode decoding, sequence alignment, data sifting, tallying of unique molecular indices, and consolidation of sequencing data were executed using version 1.2 of the Cell Ranger suite.

Subsequent analyses were conducted within the R environment (version 4.3.2), employing the Seurat toolkit (version 5.0.1) for data processing. Cells exhibiting elevated expression of multiple cluster-specific marker genes were omitted, suggesting potential polyploidy based on gene expression patterns. Additionally, cells with gene counts below 200 or exceeding 7000, along with those showing mitochondrial-encoded transcripts comprising over 10% of the total library, were excluded. Find Variable Features was utilized to pinpoint genes with significant variability, subsequently selecting the 2000 most fluctuating genes for execution in principal component analysis. Uniform Manifold Approximation and Projection (UMAP) was employed to condense the data dimensions, thereby rendering the deduced cellular groupings discernible, which were derived from an analysis of the fifteen most salient principal components.

Immunocyte types were distinguished by comparing gene expression across clusters with the Wilcoxon test, then aligning the most variant genes with established immunocyte markers to create a standardized marker set for 10 clusters.

We systematically investigated intercellular communication networks using CellChat, a computational framework for analyzing ligand-receptor interactions, applied to scRNA-seq data from *Aebp1* cKO and WT tumors. The workflow involved three sequential phases: first, preprocessing raw sequencing data and constructing genotype-specific CellChat objects; second, calculating interaction probabilities using the tool's curated ligand-receptor interaction database to quantify communication likelihoods; third, performing comparative analyses of interaction network strengths and patterns between genotypes.

Spatial transcriptomics data analysis

The stRNA-seq slides of two human COAD samples were printed with two identical capture regions. The Visium Spatial platform was employed under the default protocol to capture gene expression information in the ST slides by combining spatial barcodes with mRNA oligonucleotides. The raw sequencing reads of stRNA-seq underwent quality checking and alignment using Space Ranger (version 1.1). Subsequently, the gene-spot matrix derived from processing the ST and Visium samples was analyzed with Seurat (version 5.0.1) in R. A detection threshold of 200 was established for genes in individual spots, leading to the exclusion of genes with fewer than 10 reads or those detected in less than three spots. Spot normalization was conducted using the LogVMR method. Dimensionality reduction and clustering using the top 30 principal components were performed with Independent Component Analysis (PCA) at a resolution of 0.8. Finally, the SpatialFeaturePlot function in Seurat was utilized to create a spatial feature expression plot. The library preparation was completed, followed by sequencing on the NovaSeq 6000 system.

Real-time quantitative PCR

WT, $Aebp1^{-/-}$ mCAFs, alongside shNC/shAEBP1 mCAFs and hCAFs, were grown in DMEM for 48 hours prior to RNA extraction with Trizol reagent (15596026, Invitrogen). Subsequently, the RNA was converted to cDNA using Superscript III and generic primers, following the manufacturer's guidelines. This cDNA was then used for amplifying specific gene transcripts via qPCR with SYBR Green I Master Mix on an ABI PRISM 7300HT analyzer. For standardization purposes, glyceraldehyde-3-phosphate dehydrogenase (GAPDH) was selected as a reference gene. The primer sequences used were as follows:

Mouse *Gapdh*,

F: 5′-AGGTCGGTGTGAACGGATTTG-3′. R: 5′-TGTAGACCATGTAGTTGAGGTCA-3′.

Mouse *Cd274*,

F: 5′-GCTCCAAAGGACTTGTACGTG-3′. R: 5′-TGATCTGAAGGGCAGCATTTC-3′.

Human *GAPDH*,

F: 5′-ACAACTTTGGTATCGTGGAAGG-3′. R: 5′-GCCATCACGCCACAGTTTC-3′.

Human *PD-L1*,

F: 5′-TGGCATTTGCTGAACGCATTT-3′. R: 5′-TGCAGCCAGGTCTAATTGTTTT-3′.

Co-culture with T cells in vitro

Spleens from C57BL/6 mice were filtered through a 40-μm mesh to yield a homogenous cell suspension. Post-erythrocyte lysis, cells were enumerated and cultured in Roswell Park Memorial Institute (RPMI) 1640. Human blood was layered onto Ficoll (abs930, Absin) and centrifuged (acceleration 1/deceleration 0) to isolate peripheral blood mononuclear cell (PBMCs) from the interface layer. Prior to T cell stimulation, 12-well plates were coated with anti-CD3 (17A2 for mouse, OKT3 for human, Invitrogen) and anti-CD28 (37.51 for mouse, CD28.2 for human, Invitrogen) at 2.5 and 3 μg/ml, respectively. After 48 hours, T cells were co-cultured with CAFs, and then harvested post another 48 hours for flow cytometry.

Bioinformatics

In the TME, we performed pathway enrichment using the KEGG database via R clusterProfiler (v4.10.0) to pinpoint pathways linked to

AEBP1. GSEA (v4.0.3) was applied for further analysis, complemented by Seurat's capabilities in processing single-cell RNA sequencing (scRNA-seq) data. Significance was determined for terms with a p value < 0.05 and at least 3 enriched genes.

Western blot

Cells were lysed in ice-cold buffer containing 20 mM Tris-HCl pH 7.0, 250 mM NaCl, 1% Triton X-100, 0.5% NP-40, 3 mM EDTA, and protease inhibitors. Lysates were resolved by SDS-PAGE, transferred to nitrocellulose membranes, and blocked with 5% milk for 30 minutes at room temperature. Membranes were incubated overnight at 4 °C with primary antibodies, followed by 1-hour room temperature incubation with HRP-conjugated secondary antibodies. Protein signals were visualized using enhanced chemiluminescence reagent (34580, Thermo). The primary antibodies used in this study included anti-AEBP1 (ab254973, Abcam, 1:1000; sc-271374, Santa, 1:1000), anti-CKAP4 (sc-393544, Santa, 1:1000), anti-AKT (4691, Cell Signaling Technology, 1:1000), anti-p-AKT (4060, Cell Signaling Technology, 1:1000), anti-GAPDH (60004-1-Ig, Proteintech, 1:10000).

Co-immunoprecipitation and mass spectrometry

Cells (human/mouse CAFs and 293 T) were lysed in IP buffer, and supernatants were pre-cleared with Protein A/G beads. For immunoprecipitation, CAF lysates were incubated with 2.5 μg anti-AEBP1 (sc-271374; Santa Cruz) while 293 T lysates received anti-HA (M20003S; Abmart), with IgG (B30010S; Abmart) as control. After overnight rotation (4 °C), Protein A/G beads were added (2 h), washed with IP buffer, and eluted in SDS loading buffer for western blot. For mass spectrometry, mCAF samples were electrophoresed, Coomassie-stained (P0017; Beyotime), and analyzed by Shanghai Huaying Biotechnology Co., Ltd. (China).

Docking-based virtual screening and molecular docking

A software package from Schrödinger (Schrödinger, LLC, New York, 2015) was utilized for virtual screening of small-molecule inhibitors targeting the AEBP1-CKAP4 interaction. The protein structure preparation involved the use of the Prep Wiz module, while the identification of active sites, defined as docking pockets, was done using the SiteMap module. Screening of compounds from Chembridge and Chemdiv libraries excluded PAINS compounds through the Canvas 1.1 program. ADME properties were predicted with the QikProp 3.2 program. Molecular docking employed the Glide algorithm and analysis was based on docking scores. Cluster analysis was conducted using FCFP_6 fingerprints. The most effective small-molecule inhibitor was identified, and its mechanism of inhibition was investigated. Protein-protein docking calculations were carried out with the ZDOCK module in Discovery Studio 4.0 software. Suggestions for edits to avoid plagiarism include paraphrasing and restructuring sentences, which maintain the original content without textual duplication. The compounds were sourced from the commercial chemical libraries of ChemDiv (San Diego, CA, USA) and ChemBridge Corporation (San Diego, CA, USA).

BioRender statement

Some figures were generated using BioRender.com (Fig. 1A, 7A). Publication licenses were secured in compliance with BioRender's academic licensing terms, and appropriate attribution is provided within the corresponding figure legends.

Statistics

Data were statistically analyzed using GraphPad Prism (version 8.4.0) and R (version 4.3.2). Significance was calculated using an unpaired student t-test unless otherwise specified. For comparisons involving more than two groups, one-way ANOVA with Dunnett's or Tukey's multiple comparisons test, or two-way ANOVA with Sidak's or Tukey's multiple comparisons test were applied. Survival analysis utilized the log-rank test. A significance level of $p < 0.05$ was deemed statistically significant, with exact p values displayed on all graphs. Data were presented as mean ± SEM.

Reporting summary

Further information on research design is available in the Nature Portfolio Reporting Summary linked to this article.

Data availability

The human mRNA-seq data have been deposited in BIG Sub under the accession code HRA012427, HRA012423, stRNA under the accession code HRA008670. The mouse mRNA-seq data have been deposited in BIG Sub under the accession code CRA019349, scRNA-seq under the accession code CRA019202. The mass spectrometry (MS) proteomics data have been deposited in the ProteomeXchange database via the PRIDE partner repository under the dataset identifiers PXD067349. All data supporting the findings described in this manuscript are available in the article and in the Supplementary Information and from the corresponding author upon request. Source data are provided with this paper.

References

1. Thommen, D. S. & Schumacher, T. N. T cell dysfunction in cancer. *Cancer Cell* **33**, 547–562 (2018).
2. Paijens, S. T., Vledder, A., de Bruyn, M. & Nijman, H. W. Tumor-infiltrating lymphocytes in the immunotherapy era. *Cell Mol. Immunol.* **18**, 842–859 (2021).
3. Biffi, G. & Tuveson, D. A. Diversity and biology of cancer-associated fibroblasts. *Physiol. Rev.* **101**, 147–176 (2021).
4. Vinay, D. S. et al. Immune evasion in cancer: mechanistic basis and therapeutic strategies. *Semin. Cancer Biol.* **35**, S185–S198 (2015).
5. Mao, X. et al. Crosstalk between cancer-associated fibroblasts and immune cells in the tumor microenvironment: new findings and future perspectives. *Mol. Cancer* **20**, 131 (2021).
6. Majdalawieh, A. F., Massri, M. & Ro, H. S. AEBP1 is a novel oncogene: mechanisms of action and signaling pathways. *J. Oncol.* **2020**, 8097872 (2020).
7. Corano Scheri, K., Lavine, J. A., Tedeschi, T., Thomson, B. R. & Fawzi, A. A. Single-cell transcriptomics analysis of proliferative diabetic retinopathy fibrovascular membranes reveals AEBP1 as fibrogenesis modulator. *JCI Insight* **8**, e172062 (2023).
8. Xing, Y. et al. AEBP1, a prognostic indicator, promotes colon adenocarcinoma cell growth and metastasis through the NF-κB pathway. *Mol. Carcinog.* **58**, 1795–1808 (2019).
9. Ju, G. et al. AEBP1 promotes papillary thyroid cancer progression by activating BMP4 signaling. *Neoplasia* **49**, 100972 (2024).
10. O'Donnell, J. S., Massi, D., Teng, M. W. L. & Mandala, M. PI3K-AKT-mTOR inhibition in cancer immunotherapy, redux. *Semin. Cancer Biol.* **48**, 91–103 (2018).
11. Suchitha, G. P., Balaya, R. D. A., Raju, R., Keshava Prasad, T. S. & Dagamajalu, S. A network map of cytoskeleton-associated protein 4 (CKAP4) mediated signaling pathway in cancer. *J. Cell Commun. Signal* **17**, 1097–1104 (2023).
12. Chhabra, Y. & Weeraratna, A. T. Fibroblasts in cancer: unity in heterogeneity. *Cell* **186**, 1580–1609 (2023).
13. Zhang, Z. et al. Cancer-associated fibroblasts-derived CXCL12 enhances immune escape of bladder cancer through inhibiting P62-mediated autophagic degradation of PDL1. *J. Exp. Clin. Cancer Res.* **42**, 316 (2023).
14. De Jaeghere, E. A., Denys, H. G. & De Wever, O. Fibroblasts fuel immune escape in the tumor microenvironment. *Trends Cancer* **5**, 704–723 (2019).
15. Hosein, A. N., Brekken, R. A. & Maitra, A. Pancreatic cancer stroma: an update on therapeutic targeting strategies. *Nat. Rev. Gastroenterol. Hepatol.* **17**, 487–505 (2020).

16. Li, Y. X. et al. ACLP promotes activation of cancer-associated fibroblasts and tumor metastasis via ACLP-PPARγ-ACLP feedback loop in pancreatic cancer. *Cancer Lett.* **544**, 215802 (2022).
17. Sekiguchi, S. et al. ACLP activates cancer-associated fibroblasts and inhibits CD8+ T-cell infiltration in oral squamous cell carcinoma. *Cancers* **15**, 4303 (2023).
18. Li, X. et al. Single-cell RNA sequencing reveals a pro-invasive cancer-associated fibroblast subgroup associated with poor clinical outcomes in patients with gastric cancer. *Theranostics* **12**, 620–638 (2022).
19. Mucciolo, G. et al. EGFR-activated myofibroblasts promote metastasis of pancreatic cancer. *Cancer Cell* **42**, 101–118.e11 (2024).
20. You, T. et al. POSTN secretion by extracellular matrix cancer-associated fibroblasts (eCAFs) correlates with poor ICB response via macrophage chemotaxis activation of Akt signaling pathway in gastric cancer. *Aging Dis.* **14**, 2177–2192 (2023).
21. Nicolas, A. M. et al. Inflammatory fibroblasts mediate resistance to neoadjuvant therapy in rectal cancer. *Cancer Cell* **40**, 168–184.e13 (2022).
22. Macy, A. M., Herrmann, L. M., Adams, A. C. & Hastings, K. T. Major histocompatibility complex class II in the tumor microenvironment: functions of nonprofessional antigen-presenting cells. *Curr. Opin. Immunol.* **83**, 102330 (2023).
23. Hu, B. et al. Subpopulations of cancer-associated fibroblasts link the prognosis and metabolic features of pancreatic ductal adenocarcinoma. *Ann. Transl. Med.* **10**, 262 (2022).
24. Reschke, R. & Gajewski, T. F. CXCL9 and CXCL10 bring the heat to tumors. *Sci. Immunol.* **7**, eabq6509 (2022).
25. Bill, R. et al. CXCL9:SPP1 macrophage polarity identifies a network of cellular programs that control human cancers. *Science* **381**, 515–524 (2023).
26. Sun, C., Mezzadra, R. & Schumacher, T. N. Regulation and function of the PD-L1 checkpoint. *Immunity* **48**, 434–452 (2018).
27. Kim, D. K. et al. PD-L1-directed PlGF/VEGF blockade synergizes with chemotherapy by targeting CD141^{+} cancer-associated fibroblasts in pancreatic cancer. *Nat. Commun.* **13**, 6292 (2022).
28. Yi, M., Niu, M., Xu, L., Luo, S. & Wu, K. Regulation of PD-L1 expression in the tumor microenvironment. *J. Hematol. Oncol.* **14**, 10 (2021).
29. Chen, H. et al. DKK1 activates the PI3K/AKT pathway via CKAP4 to balance the inhibitory effect on Wnt/β-catenin signaling and regulates Wnt3a-induced MSC migration. *Stem Cells* **42**, 567–579 (2024).
30. Nagoya, A. et al. CKAP4 is a potential exosomal biomarker and therapeutic target for lung cancer. *Transl. Lung Cancer Res.* **12**, 408–426 (2023).
31. Song, J. W. et al. GOLPH3/CKAP4 promotes metastasis and tumorigenicity by enhancing the secretion of exosomal WNT3A in non-small-cell lung cancer. *Cell Death Dis.* **12**, 976 (2021).
32. Layne, M. D. et al. Impaired abdominal wall development and deficient wound healing in mice lacking aortic carboxypeptidase-like protein. *Mol. Cell Biol.* **21**, 5256–5261 (2001).
33. Li, D., Liu, Z., Ding, X. & Qin, Z. AEBP1 is one of the epithelial-mesenchymal transition regulatory genes in colon adenocarcinoma. *Biomed. Res. Int.* **2021**, 3108933 (2021).
34. Sinha, S. et al. AEBP1 down regulation induced cell death pathway depends on PTEN status of glioma cells. *Sci. Rep.* **9**, 14577 (2019).
35. Sharma, P. et al. Immune checkpoint therapy-current perspectives and future directions. *Cell* **186**, 1652–1669 (2023).
36. Jiang, P. et al. Signatures of T cell dysfunction and exclusion predict cancer immunotherapy response. *Nat. Med.* **24**, 1550–1558 (2018).
37. Kaneda, M. M. et al. PI3Kγ is a molecular switch that controls immune suppression. *Nature* **539**, 437–442 (2016).

Acknowledgements

This work was supported by the National Natural Science Foundation of China (Nos. 82173166, 82372886, 81472475 to H.L., 82372996 to F.L., and 82303296 to J.L.), Natural Science Foundation of Chongqing (cstc2021jcyj-msxmX0015 to H.L.), and Chongqing Graduate Tutor Team Construction Project, Chongqing Education Commission Foundation (cqmudstd202216 to H.L.), CQMU Program for Youth Innovation in Future Medicine (No. W0094 to H.L.), and GuangDong Basic and Applied Basic Research Foundation (2022A1515111217 to J.L.).

Author contributions

X.W., J.L., D.S., Y.W., J.Z.L.: conceptualization, visualization, data curation, Validation, writing—original draft, formal analysis. Z.Y., J.S., J.H., L.W.: visualization, methodology, investigation. X.Z., J.W., L.Z., F.L., Y.W., Y.Z., H.D. C.L.: software, resources, methodology. J.L., F.L., H.L.: foundation. G.R., H.L.: writing—review & editing, conceptualization, supervision, project administration. All authors made substantial contributions to acquisition of data, critically revised the manuscript, and gave final approval of the manuscript to be submitted.

Competing interests

The authors declare no competing interests.

Additional information

Supplementary information The online version contains supplementary material available at https://doi.org/10.1038/s41467-025-63659-w.

Correspondence and requests for materials should be addressed to Guosheng Ren or Hongzhong Li.

Peer review information *Nature Communications* thanks Isabelle Cremer, Hiromu Suzuki and Toshihiko Torigoe for their contribution to the peer review of this work. A peer review file is available.